EIC CDR V01

August 7, 2020

Contents

Chapter 3

EIC Design

3.1 Interaction Region Design

3.1.1 Interaction Region Design Concept

The design parameters of the EIC and their rationale have been discussed in Sections **??**. Some parameters relevant for the interaction region design are repeated in Table 3.1 for convenience.

Table 3.1: Key beam parameters at the energy point of highest luminosity relevant for the interaction region design. needs still to be made consistent

	Proton	Electron	Proton	Electron	Proton	Electron
E_{CM} [GeV]	105		140		29	
Energy [GeV]	275	10	275	18	41	5
ϵ_x [nm]	9.6	20.0	15.8	24.0	43.6	20.0
ϵ_y [nm]	1.5	1.2	2.5	2.0	10.3	3.5
β_x^* [cm]	90	43	90	59	90	196
β_y^* [cm]	4.0	5.0	4.0	5.0	7.1	21.0

The purpose of the interaction region (IR) is to focus the beams to small spot sizes at the collision point and to separate them into their respective beam lines while providing the space and geometry required by the physics program for the detector. The separation is accomplished by a total crossing angle of 25 mrad between the two beams, which has the advantage of avoiding the introduction of separator dipoles in the detector vicinity that would generate huge amounts of synchrotron radiation. The detrimental effects of this crossing angle on the luminosity and beam dynamics are compensated by a crab-crossing

scheme. Figure 3.1 shows a zoom in of the rear and forward side of the IR.

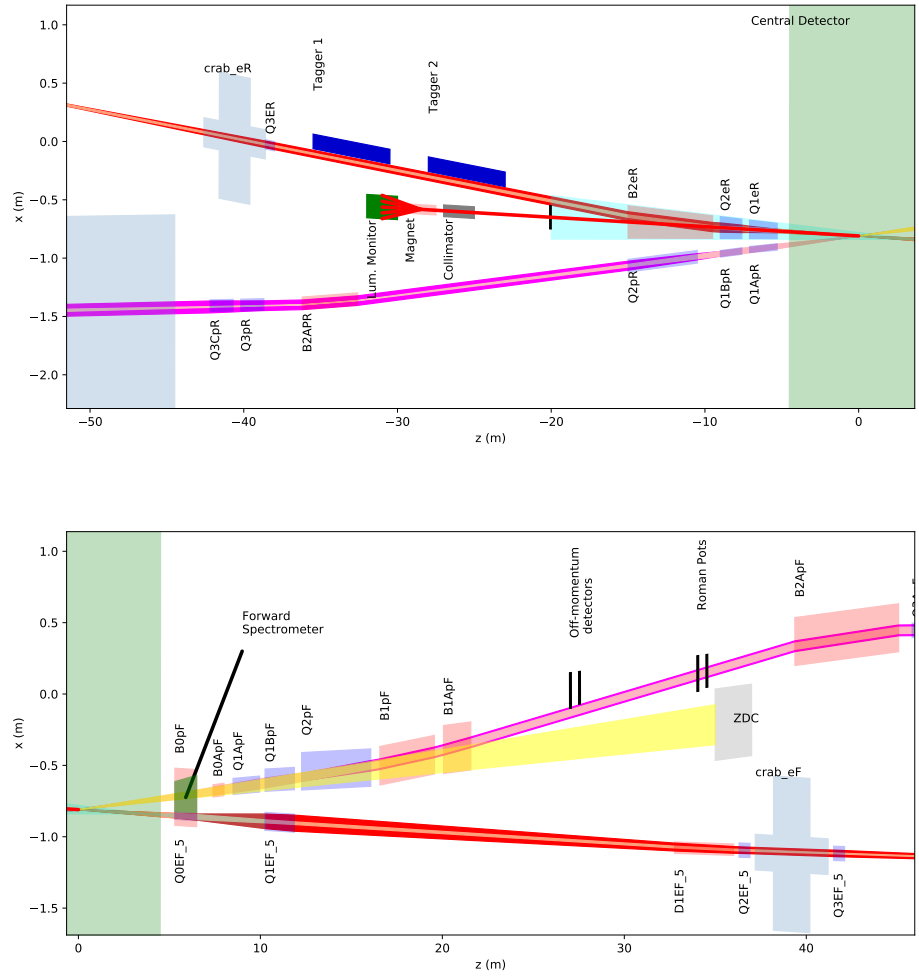

Figure 3.1: A zoom of the interaction region layout in the rear (top) and forward (bottom) directions.

The layout of the interaction region (IR) fulfills the following requirements:

- To achieve high luminosity, small beam cross sections are required. The beams are strongly focused at the interaction point (small β^*) by low-β-quadrupole magnets (also referred to as final focusing quadrupoles).
- The final focusing quadrupoles must have sufficient aperture for the large beam size at their location.
- Large contributions to the chromaticity, which is a set of parameters characterizing the energy sensitivity of the beam optics, are generated in the low-β quadrupoles.

Chromaticity needs to be compensated by nonlinear sextupole fields which, in turn, limit the dynamic aperture. The IR design balances small β^* and tolerable values of chromaticity.

- The colliding beam detector requires a large acceptance of protons scattered off the collision point. Therefore, we do not place accelerator components inside the detector (± 4.5 m from the IP). Some of the low-β quadrupoles have even larger apertures so that scattered protons and neutrons can be detected by detector elements placed further downstream.

- The beam divergence (and the minimum β^*) is restricted to enable detection of forward scattered protons with transverse momentum as small as $p_t = 200\,\mathrm{MeV/c}$. These particles are then outside the $10\,\sigma$ proton beam envelope and are detectable by near-beam-detectors, "Roman Pots", which are placed along the forward hadron beam pipe.

- The beams collide under a crossing angle of 25 mrad to separate the electron and proton beams quickly, to avoid parasitic collisions and to provide space for a neutron detector at zero degree in the forward [1] direction and the luminosity detector in the in the rear side where the electron exit. An important factor is the large bunch frequency (up to 99 MHz, which corresponds to only 10 ns bunch spacing) required for high luminosity. The crossing angle effects (enlarged transverse beam size and excitation of synchro-betatron resonances) must be compensated for by using crab cavities, transverse RF resonators which kick the head and the tail of the proton (and electron) bunches in opposite directions in the plane of the crossing angle. These cavities are placed at a horizontal betatron phase advance of $\pi/2$ from the interaction point (IP) on both the rear- and the forward sides, forming a 180° bump. This causes the bunches to be tilted in the horizontal plane by exactly half the crossing angle at the IP, and provides (ideally) the same collision geometry as head-on collisions and thereby avoids synchrobetatron coupling.

- Strong synchrotron radiation, which might be generated by the electron beam, can destroy sensitive detector equipment and make data-taking impossible. Therefore, we argue that the electron beam must not experience dipole fields in the interaction region (IR), and certainly not upstream of the IP (we use the term forward side). This is another strong reason why the two beams must collide at a crossing angle. Synchrotron radiation generated in the low-β quadrupoles on the rear-electron side should be absorbed on the rear side of the IR as far as possible from the detector so as to minimize backscattered photons. This requires an extra large aperture for the electron low-β quadrupole magnets on the downstream side of the IP.

- Both the light hadron and electron beams are spin polarized. Polarization is only stable if the polarization direction coincides with the direction of the guide field in the arc. In collisions, the spins of the electron beam are oriented longitudinally and the ones for the hadron beam either longitudinally or transverse. Thus the IR design

[1] The IP separates the IR into a forward and a rear side or direction. The forward side is the side of the proton beam coming from the IP and the rear side is the side of protons going to the IP.

accommodates pairs of spin rotators, which ensures longitudinal spin at the IP and vertical spin in the arcs. The spin rotators in the hadron ring already exist and are unchanged in this design. The spin rotators for the electron beam consist of two pairs of strong solenoids with quadrupole magnets in-between each pair which are tuned such that the x-y coupling by the two solenoids cancels. This set of four solenoids is required on both sides of the IP. The beam transport between the rotators is "spin transparent". This means that the magnetic fields in quadrupole magnets experienced by a particle performing betatron and synchrotron oscillations cancel between the spin rotators.

- The IR layout must provide room for a luminosity monitor on the rear side. This monitor detects hard γ-rays that are generated in the Bethe-Heitler process and exploited for luminosity measurement. The dipole magnet bending the electrons away from the path of the γ beam is at the same time a spectrometer magnet for the off-momentum electrons generated at low Q^2.

- On the forward proton side, a neutron spectrometer is required. A dipole magnet bends the hadron beam away from the collision axis to provide space for this element. It also generates dispersion which helps to detect forward scattered protons in detectors that are integrated into the hadron beam pipe (called "Roman Pots")

The small β-functions at the IP necessitate focusing elements as close as possible to the IP. This is accomplished by a combination of dual-aperture magnets and single-aperture quadrupoles with field-free regions for the electron beam, as shown in Figures 3.2. Design magnet apertures are chosen such that a minimum aperture radius of 10σ for protons and 15σ for electrons is ensured in all operating modes. Tables 3.2 to 3.4 list the magnet parameters in the electron and proton beam lines and their positions, beginning from the interaction point (IP).

Table 3.2: Forward hadron magnets, the settings are for 275 GeV.

FORWARD DIRECTION	Hadron Magnets						
	B0PF	B0APF	Q1APF	Q1BPF	Q2PF	B1PF	B1APF
Center position [m]	5.9	7.7	9.23	11.065	14.170	18.070	20.820
Length [m]	1.2	0.6	1.46	1.6	3.8	3.0	1.5
Center position w.r.t. to x-axis [cm]	-1.50	5.5	1.40	2.38	4.07	3.90	8.00
Angle w.r.t. to z-axis [mrad]	-25.0	0.0	-5.5	-10.0	-10.2	9.0	0.0
Inner radius [cm]	20.0	4.3	5.6	7.8	13.1	13.5	16.8
Peak field [T]	-1.3	-3.3	0.0	0.0	0.0	-3.4	-2.7
Gradient [T/m]	0.0	0.0	-72.608	-66.180	40.737	0.0	0.0

Since for both beams the vertical IP β-function is much smaller than the horizontal one, $\beta_y^* \ll \beta_x^*$, the innermost quadrupoles on both beam lines are vertically focusing. In the hadron ring this limits the maximum vertical β-function in those magnets to about 1600 m

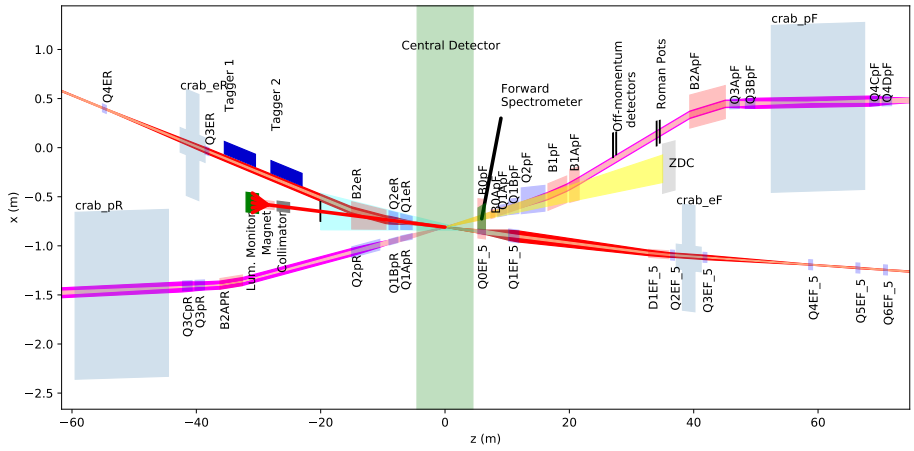

Figure 3.2: Schematic layout of the interaction region (top view, as simulated for high divergence, no cooling). Beams cross with a crossing angle of 25 mrad. Note the length scales for the horizontal and vertical axis are very different. The IR design integrates focusing magnets for both beams, luminosity and neutron detectors, electron taggers, spectrometer magnets, near-beam detectors (Roman pots for hadrons), crab cavities, and spin rotators for both beams. The two beams are both focused by quadrupole doublets. On the hadron-forward side, there are separate focusing magnets, which are longitudinally interleaved. The first quadrupole magnet for electrons is integrated into a hadron spectrometer dipole. On the rear side, hadrons and electrons are focused by quadrupoles, which are installed side-by-side in the same cryostat. The maximum β-functions in the IR for hadrons of 2000 m remain within the operating range of RHIC, while the maximum β-functions for electrons remain below 500 m.

at a proton beam energy of 275 GeV, resulting in moderate contributions to the overall chromaticity of the machine. The horizontal β-function is intentionally increased to about 1300 m in the region of the crab cavities. This limits the required voltage of those devices, which scales as $1/\sqrt{\beta_x^* \beta_{\mathrm{crab},x}}$, to about $U_{\mathrm{crab}} = 12\,\mathrm{MV}$. At lower energies the IP β-functions are increased, resulting in lower β-functions in the low-β magnets as well as at the crab cavities. However, due to the lower beam rigidity the required crab cavity voltage does not exceed 14 MV at any energy.

The focusing scheme for the electrons is conceptually the same as for the hadrons. The vertical β-function reaches a maximum of about 500 m in the low-β quadrupoles, while the horizontal β is intentionally increased to about 200 m at the crab cavities to limit their required voltage.

The forward hadron magnet apertures are completely dominated by experimental acceptance requirements, and the $10\,\sigma$ outline shown for the circulating beam only uses the small central regions of the magnet apertures. This allows particles scattered at small angles to pass through the apertures of the innermost magnets so they can be detected by detectors which are integrated into the hadron beam vacuum system ("Roman Pots") further down the beamline.

Table 3.3: Forward electron magnets, the settings are for 18 GeV electron beam energy.

FORWARD DIRECTION	Electron Magnets		
	Q0eF	Q1eF	D1eF
Center position [m]	5.9	11.065	34.389
Length [m]	1.2	1.61	3.238
Angle w.r.t. to z-axis [mrad]	25.0	25.0	25.0
Inner radius [cm]	2.50	6.3	NA
Peak field [T]	0.0	0.0	0.067
Gradient [T/m]	-14.05	6.2624	

Table 3.4: Rear hadron and electron quadrupoles with their apertures tapered in proportion to their distance to the IP for 275 GeV and 18 GeV, respectively.

REARWARD DIRECTION	Hadron Magnets			Electron Magnets		
	Q1APR	Q1BPR	Q2PR	Q1eR	Q2eR	B2ER
Center position [m]	-6.2	-8.30	-12.75	-6.2	-8.30	-12.25
Length [m]	1.80	1.40	4.50	1.80	1.4	5.50
Angle w.r.t. to z-axis [mrad]	0.0	0.0	0.0	25.0	25.0	25.0
Entrance radius [cm]	2.00	2.80	5.40	6.60	8.30	9.70
Exit radius [cm]	1.00	1.00	1.00	1.00	1.00	1.00
Peak field [T]	0.0	0.0	0.0	0.0	0.0	-0.198
Gradient [T/m]	-78.375	-78.375	33.843	-13.980	14.100	0.0

The B0 spectrometer magnet shown in Figure 3.3 is used to cover an intermediate experimental acceptance region below what can be detected in the main solenoid detector and above particle angles that will exit through the IR magnets. Inside its aperture the electron beam is shielded by a 2 m long superconducting bucking coil (dipole active shield magnet) with an outside diameter of 10 cm and a field of 1.3 T. This bucking coil houses the vertically focusing superconducting electron low-β quadrupole Q1EF, as shown on Figure 3.4. There is currently an effort going on to further optimize the B0-design, a detailed update will be available by CD-1.

The B1PF and B1APF dipoles separate the hadron beam from the outgoing 4 mrad neutron cone, and create dispersion at the Roman Pots to allow determination of the forward momentum of the scattered particles.

The electron beamline on the forward side does not contain any bending magnets within 80 m upstream of the IP. Within this region the only source of synchrotron radiation is fo-

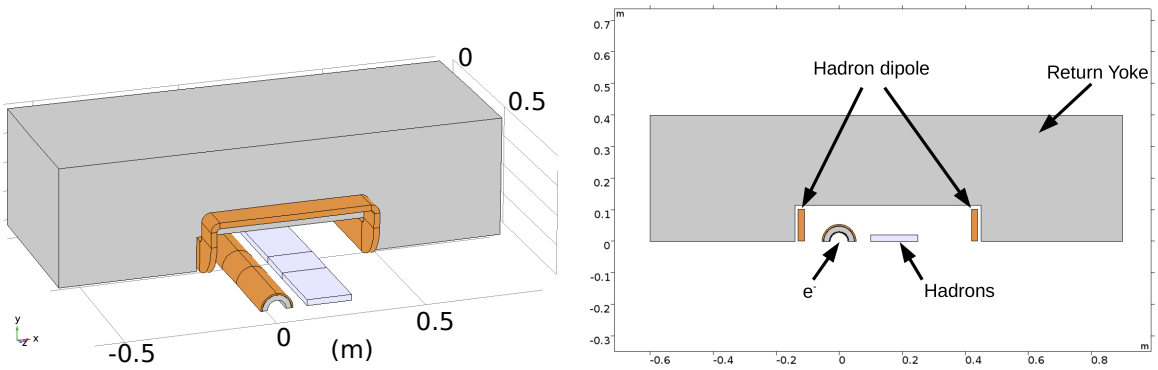

Figure 3.3: Schematic drawing of the warm iron B0 spectrometer dipole with the superconducting 1.3 T bucking coil shielding the electron beam, and the electron quadrupole Q1EF inside that bucking coil

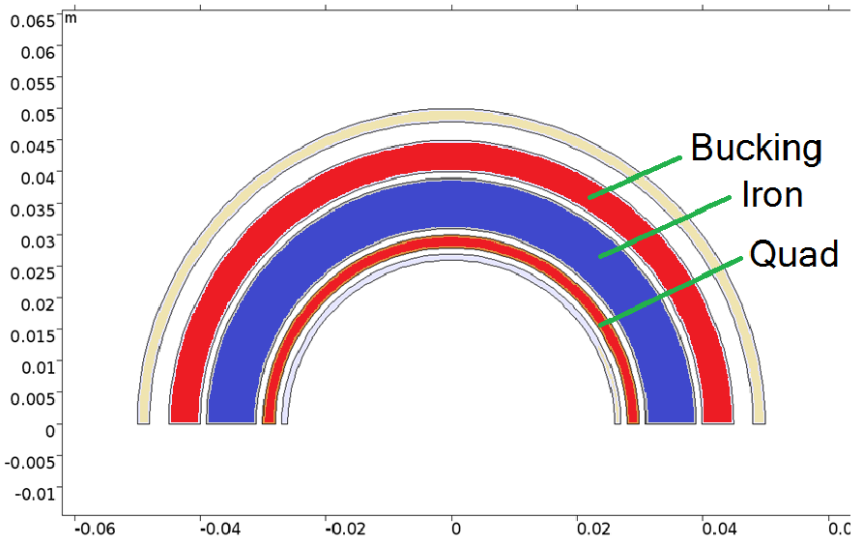

Figure 3.4: Design of the electron quadrupole Q1EF with its 1.3 T bucking coil to shield the electron beam from the B0 spectrometer magnet.

cusing in quadrupole magnets. The synchrotron radiation fan generated in the far away arc dipoles can be easily collimated such that it is completely contained within the radiation fan produced by the quadrupoles in the straight. This fan has finite maximum divergences, collimated to $13\,\sigma$ bounds, that are allowed to pass without interference through the beam pipe and following magnets, thus allowing for installation of detector components close to the beam. This is discussed in detail in Section 3.1.6.

On the rearw side, no dipoles are introduced into the proton beam line, which allows placement of the low-β quadrupoles even closer to the IP than on the forward side. The electron beamline contains a bending magnet that bends the electrons away from the γ-beam generated by scattering of electrons at the hadrons (Bethe-Heitler process) which is used to measure luminosity in the luminosity monitor placed in this area. The bending magnet

also serves as a spectrometer to tag scattered electrons that lost energy in the Bethe-Heitler process, but most importantly for the scattered electrons with low Q^2. However, since this magnet is introduced downstream of the main detector the associated synchrotron radiation fan does not pass through the experiment.

The vertically focusing low-β quadrupoles Q1ER and Q1APR as well as Q2ER and Q1BPR are realized as superconducting dual-aperture magnets sharing the same iron yoke, as shown in Figure 3.5 (left). The apertures for both beams are tapered and angled with respect to each other, following the divergent proton beam and synchrotron radiation fan as they emerge from the central detector, as depicted in Figure 3.5 (right). The tapering is needed to minimize the initial magnet apertures and to allow enough iron between the beams in order to limit the magnetic fields for each of them effecting the other section.

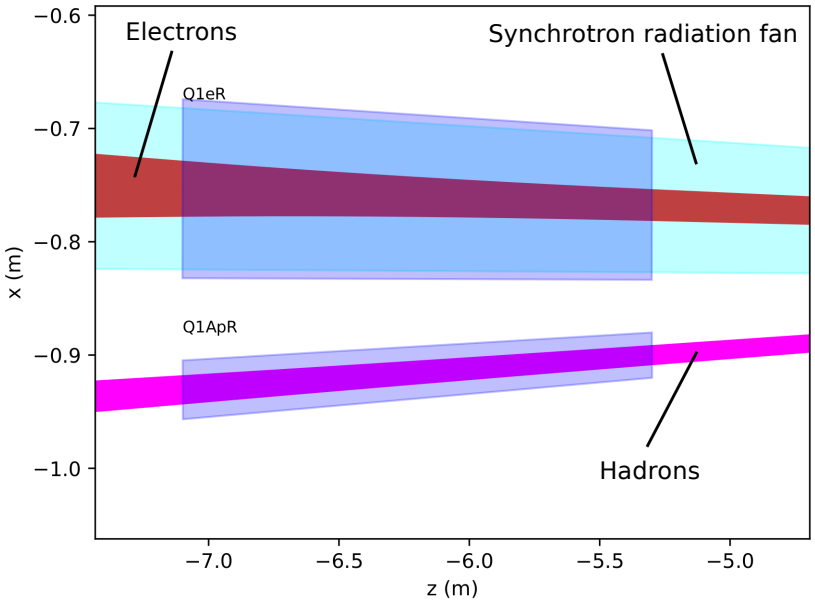

Figure 3.5: Cross section and top view of the first rear quadrupoles Q1ER and Q1PR, sharing the same iron yoke. The apertures are tapered around the synchrotron radiation fan and the proton beam envelope, respectively.

The required horizontal aperture radius x_{synch} to accommodate the synchrotron radiation fan from the 12.5σ electron beam at distance s from the IP is parametrized as

$$x_{\text{synch}}(s) = 6.75 \times 10^{-3}(s + 3.5) \tag{3.1}$$

This was used for the initial design of the magnets; using masks the rear electron magnet apertures can be substantially reduced as shown in section 3.1.6.

The vertical size of the synchrotron radiation fan y_{synch} is significantly smaller than the horizontal one. The horizontally focusing quadrupoles Q2ER (tapered) and Q2PR (not

tapered) are conceptually similar to Q1ER and Q1APR. With these apertures, the entire synchrotron radiation fan is transported safely through the interaction region until it hits a dedicated absorber 23 m from the IP. Recently much more detailed simulations based with the SYNRAD code have been done and are described in section 3.1.6.

It is noted that the EIC has the capability of having two interaction regions (IRs). There is complementarity in the design of the two IRs with respect to the center-of-mass energy range where the 2nd IR is optimized to have the highest luminosity and detection capabilities alternative to the 1st IR. This appendix **??** discusses implementation of the 2nd IR consistent with nuclear physics, accelerator and engineering requirements. These include the operation of both IRs over the entire energy range of 29 GeV to 140 GeV center of mass. Consistently with user demands and the complementarity approach, the 2nd IR is optimized to provide the highest luminosity at a lower CM that the 1st IR, between ≈ 45 GeV and ≈ 80 GeV. This allows one to level off the luminosity curve of the EIC as a whole at a higher level over a wider energy range. It can also provide a different acceptance coverage than the 1st IR described in this chapter.

3.1.2 IR Vacuum Design

The interface requirements within the IR present several complex challenges, which require close attention to detail. The vacuum chamber in this region will become the primary interface between the particle beams and the different detector components.

One of the first challenges is to meet all of the geometrical requirements of the region. First and foremost the vacuum chamber must be designed to allow clear passage of the two high energy particle beams. Space constrains for the synchrotron radiation (SR) fan resulting from the strong focusing electron quadrupoles also need to be taken into account. Designing the central vacuum pipe with a large diameter would easily meet these requirements and it would provide a large conductance to the vacuum pumps that are required to achieve the lowest possible pressure in the detector region. However, to ensure large acceptance for all the collisions products, detectors must be placed as close as possible to the interaction point. Since these particles must pass through the walls of the beam pipe, every effort must be made to minimize their thickness.

The design is further complicated by the fact that the charged particle beams induce electromagnetic fields in the walls of the vacuum chambers. These induced fields create an image current inside the vacuum chamber walls, which travels with the particle bunches as they move through the accelerator. Changes in the material resistivity or abrupt steps result in wake fields, which can impede the image current and lead to energy loss and heating of the vacuum system.

Every effort must be made to reduce the dynamic pressure inside the IR vacuum chamber in order to minimize beam-gas interactions. The particles in the circulating beams can scatter on the residual gas molecules, which can results in high detector backgrounds. Any synchrotron radiation (direct or scattered) impinging on surfaces will result in a high dynamic pressure from photon induced desorption and surface heating. This further in-

creases the beam-gas interaction problem and the resulting background of the detectors.

Geometry

In order to define an initial acceptable envelope for the IR vacuum chamber, a full scale layout of the central detector region was developed (see Figure 3.6). It soon became clear that as a result of the shallow crossing angle between the beams, there was not adequate space for two independent beam pipes leading up to the inner detector region. In order to mitigate this problem, the decision was made to combine the two pipes into one common vacuum flange in order to save space. It also became clear that there is very little space remaining between the start of the detector region and the final focusing magnets in the forward hadron beam direction. Further work will be needed in this area to ensure all critical vacuum elements such as RF shielded bellows and UHV pumps will fit.

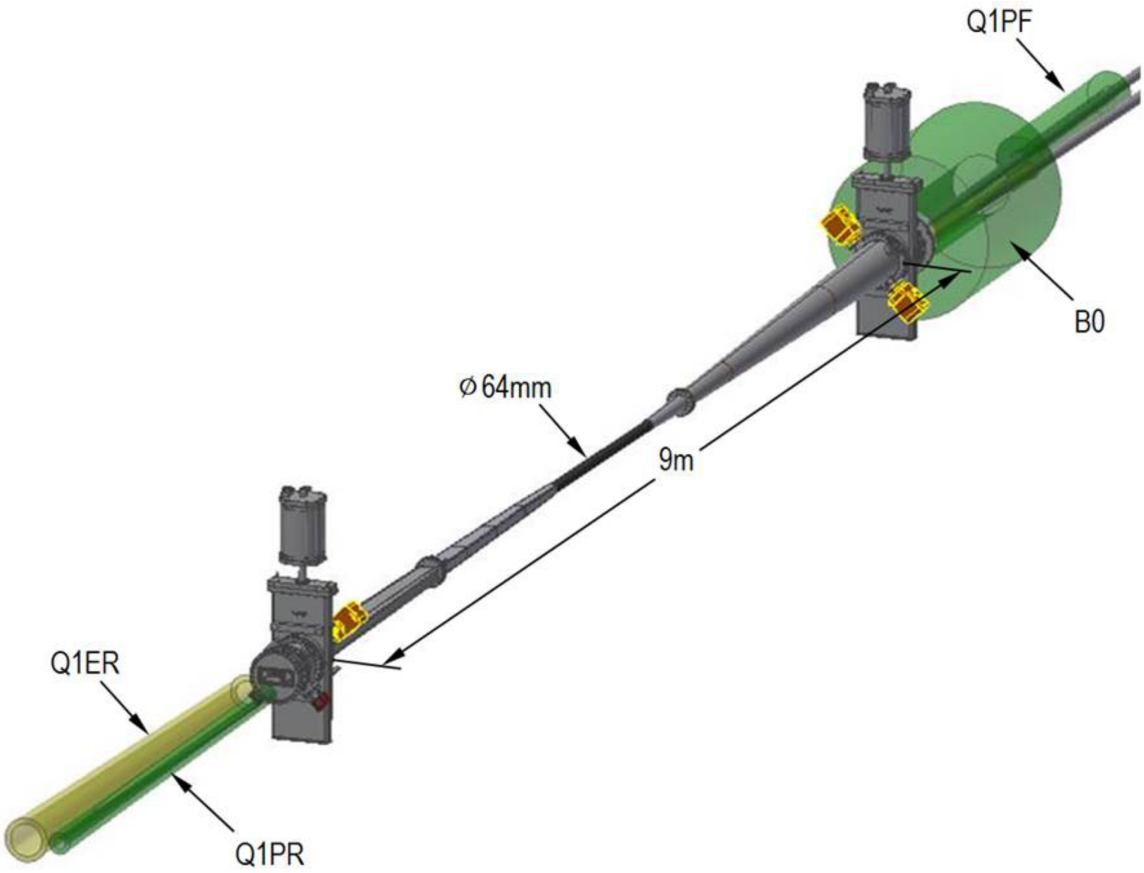

Figure 3.6: Interaction region layout with magnets. The incorporation of gate valves is still under consideration

In addition to the crossing angle, one of the leading parameters driving the size of the central beam pipe is synchrotron radiation. This radiation is produced when relativistic electrons are accelerated radially, or perpendicular to their velocity. To minimize this

problem the closest electron dipole magnet has been located as far as possible ($> 36\,\text{m}$) from the IR to leave space for collimating the radiation produced. While the dipole magnets are responsible for the majority of the synchrotron radiation, the strong final focusing electron quadrupoles located just upstream of the detector also need to be taken into account. In order to study the resulting radiation (see Figure 3.7) multiple simulation studies were performed using the SynRad software package developed at CERN [1]. A stay-clear envelope was established based on the final magnet and beam parameters which result in the highest electron beam divergence.

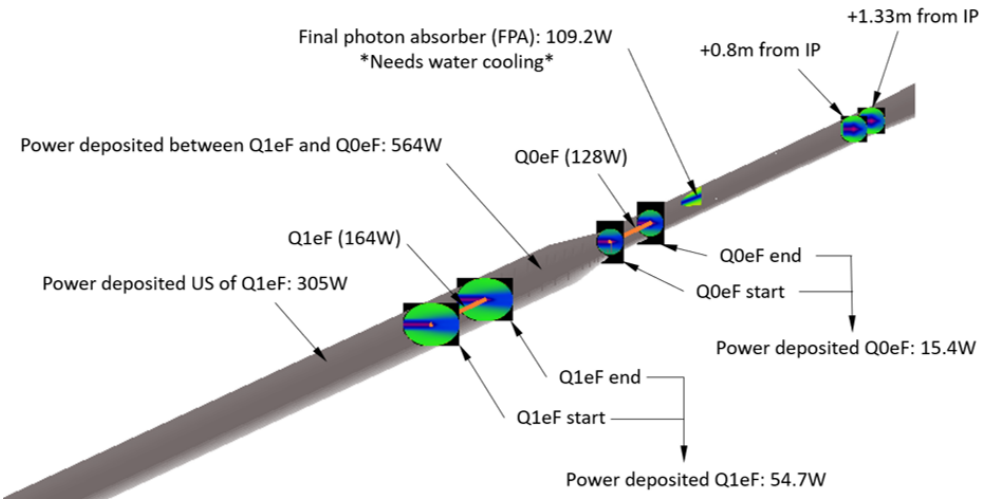

Figure 3.7: SynRad code simulation showing the resulting synchrotron radiation from the electron focusing quadrupoles Q0EF, Q1EF and DB1EF

Considering the central portion of the beam pipe will be made from beryllium and taking into account its limited fabrication possibilities, an inside diameter of 62 mm was defined. This value provides some additional clearances for mechanical and positioning tolerances. In the outgoing electron beam direction, the beam pipe will continue to increase in size to ensure the synchrotron radiation can travel through the IR without impinging on the chamber walls. In the forward hadron beam direction the beam pipe will have a conical cross section in order to provide an unobstructed path to the forward spectrometer located in the B0 magnet bore. To minimize the beam impedance for the electrons, a conducting screen will be installed which will maintain a uniform geometry for the induced image currents. Once outside the central detector region the forward traveling particles will pass through a vacuum-air interface made of thin aluminum or stainless steel before entering the B0 spectrometer. The design and position of the required chamber supports will need additional care. These supports must ensure that the chamber does not encroach into the stay clear area and must also guarantee the mechanical stability of the chamber during operations and bake out. Careful consideration to the natural frequency of the suspended system must be taken into account to avoid amplifying mechanical vibrations, which can lead to stress and fatigue of the chamber. Where possible, natural vibration frequencies will be kept above 50 Hz.

Material Considerations

To minimize the interaction of the collision products in the vacuum chamber walls, their thickness has to be kept at a minimum. The 'transparency' of a material is usually quantified through the radiation length (χ_0) for elastic collisions and the interaction length (l_T) for inelastic hadron collisions.

The radiation length is defined as the mean distance over which a high-energy electron loses all but $1/e$ of its energy by bremsstrahlung radiation. This property is inversely proportional to the density and atomic number of the material. The interaction length is the mean distance traveled before experiencing an inelastic nuclear interaction.

In order to reduce the background produced by these material properties, the walls of the vacuum chamber should be made as thin as possible. A limit is clearly defined by the mechanical integrity of the vacuum chamber. If the chamber is too thin, the vessel will collapse under the outside atmospheric pressure or fail to meet the tight mechanical tolerances required to stay clear of sensitive instrumentation. To compare the nuclear and mechanical performances of various materials, $\chi_0 E^{-1/3}$ has been used to define the figure-of-merit, with E being the Young's modulus. The required chamber wall thickness is directly proportional to $E^{-1/3}$, the properties of several materials are listed in Table 3.5.

Table 3.5: Table of material properties considered for the IR vacuum pipe.

Material	χ_0 [cm]	l_T [cm]	E [GPa]	$\chi_0 E^{-1/3}$
Beryllium	35.3	41.8	290	2.34
Carbon fiber	27.0	40.0	200	1.58
Aluminum	8.9	28.7	70	0.37
Titanium	3.6	21.4	110	0.17

While beryllium would seem to be the best choice it has several drawbacks including fabrication difficulties and safety concerns as well as having very high cost. For these reasons, only the central portion of the IR chamber will be made from beryllium. Additional aluminum sections made from AA2219 will be electron beam welded to the center section to complete the approximately 9 m long vacuum section. This particular aluminum alloy can be used at operating temperatures up to 250° C and is weldable using conventional techniques. Three separate vacuum pipes are envisioned with flange joints located at positions compatible with the central detector. The shorter pipe sections will not only simplify the fabrication, transportation and handling of the fragile chambers and also facilitate NEG coating on the interior vacuum surfaces.

The magnetic properties of materials used in the interaction region must be carefully considered. Most of the vacuum chamber components will be made of beryllium, aluminum and copper which are non-magnetic. Any stainless steel used in this region will be 316LN. This austenitic stainless steel maintains its very low magnetic permeability after welding or cold working. In general the use of stainless steel in the IR will be avoided due to the presence of cobalt in the material and the possible formation of ^{60}Co due to neutron acti-

vation. Once formed, this radioactive isotope has a half-life of 5.3 years, severely limiting the serviceability of the area.

Impedance and Instabilities

From an electromagnetic standpoint, the ultimate beam pipe would be a perfectly smooth flawless conductor. This would allow the induced image currents to travel along the chamber walls without losses or forces acting back on the particle beam. In reality this is not possible and one has resulting electromagnetic interactions, called wake fields. Longitudinal and transverse fields are generated when a bunch passes a sudden change in geometry or wall resistivity. These transverse fields can deflect the beam and lead to instabilities while the longitudinal wake fields lead to energy loss of the particles and localized heating of vacuum components.

In order to reduce effects related to resistivity changes, materials such as stainless steel pipes with small diameters will be copper plated. The required copper thickness depends on the shape of the beam pipe, distance from the beam and the average bunch current. Critical elements will be simulated to determine the minimum thickness required. To minimize detrimental effects from sudden geometry changes a radial tapering requirement of 10:1 will be followed, unless absolutely not possible. This means a 1 mm change in the radial distance between the particle beam and the chamber wall will occur over at least 10 mm of longitudinal space. RF shielding will be used to bridge all vacuum flange joints to prevent trapped modes and to help maintain uniform wall geometry. Even a few watts of deposited power on an uncooled vacuum surface can result in an extremely high temperature rise. Bellows, which need to be installed to compensate for mechanical misalignment and provide room for thermal expansion during bake outs, will also be internally shielded to avoid trapped modes. Steps inside the bellows RF shielding will be kept to a minimum.

Vacuum Requirements

Every effort must be made to reduce the residual gas pressure in the interaction region to minimize beam-gas interactions. The first concern is related to scattering, both elastic (Coulomb) and inelastic (Bremsstrahlung). Particles in the beam which are scattered off of the remaining gas molecules can further interact with vacuum chamber walls. This in turn leads to a 'positive feedback' loop which can quickly turn catastrophic. The second concern is related to phenomena such as ion induced desorption and electron multipacting. In both of these cases charged particles, freed electrons or ionized residual gas molecules are accelerated by the electric fields resulting from the charged particle beams. These accelerated particles can bombard the vacuum chamber walls and lead to large localized pressure rises and additional scattering. This is another self-feeding process. All of these mechanisms decrease the beam lifetime and intensity, influence the detector background signal and have an overall impact on the luminosity of the machine.

In order to eliminate the potential of unwanted contamination and ensure the lowest possible base pressure, best UHV practices will be followed from start to finish. This entails special processing of fabricated parts, careful surface treatment and minimizing the surface area exposed to vacuum. All parts will be chemically cleaned and/or vacuum baked prior to welding or assembly. After cleaning, no vacuum surfaces will be touched with bare hands and all openings to vacuum surfaces will be wrapped in clean vacuum grade aluminum foil.

Given the limited space for lumped pumping as well as the need for ultra-high vacuum throughout the entire interaction region, the vacuum chamber will be coated with a non-evaporative getter (NEG) layer. This coating will be magnetron sputtered directly onto the interior surfaces of the IR vacuum chambers. NEG layers are a composition of active metals (Ti, Zr and V) which chemically pump most of the gases found in a UHV system (N_2, CO and CO_2). It also has a high diffusivity for H_2 which is the predominant gas in a baked leak tight vacuum section. The film also creates a hydrogen barrier on the interior surfaces which limits the permeation of H_2 into the system. In addition to all of these benefits the film has a low secondary electron yield, which reduces the risk of electron cloud formation, and being in the order of microns, adds negligible mass between the experiment and the detectors.

Incorporating NEG coating into the design has two implications. First is the degradation of the pumping performance after successive regenerations. Anytime the vacuum section is vented for maintenance, the NEG layer becomes completely saturated and needs to be regenerated to regain its pumping characteristics. Regenerating the layer requires dissolving the surface oxides and nitrides into the bulk material which creates a new metallic surface facing the vacuum system. Since the film is thin, it has a limited storage capacity. Some of the pumping capacity can be regained by activating at higher temperatures but the upper bound is limited by the material choices for the vacuum chambers. To increase the potential number of activations, the detector vacuum section will be vented with an extremely pure noble gas which is not pumped by NEG film.

Given the limited access inside the central detector region, permanently mounted heaters are envisioned to facilitate baking. Thin polyamide heaters which are made from thin metal foils sandwiched between Kapton films will be used. These heaters can be made in almost any size or shape with varying watt densities to ensure adequate heating and activation of the NEG coatings. While adding some radiation length, these are a good compromise considering the alternatives and will only be used where removable heaters cannot be installed. Depending on the final design of the detector, additional insulation may be required to protect sensitive components located close to the beam pipe or they will need to be removed for the bake out.

Since NEG coatings only pump active gases, ion pumps will be installed at either side of the interaction region for residual noble gases. Ion pumps are Penning traps with crossed electrical and magnetic fields. The magnetic field increases the flight time of free electrons which ionize incoming gas molecules. These ions are then accelerated in the presence of the electric field and impact on a metallic cathode typically made of titanium or tantalum. This freshly sputtered material can physically or chemically react with gas present in the

system.

3.1.3 Interaction Region Performance for Scientific Requirements

The physics program of an EIC and the resulting requirements for the detector and the IR have been discussed in sections **??** and 3.1. In order to verify that the IR design fulfills all the requirements as summarized in Table **??**, an EIC general purpose detector, the auxiliary detectors, the vacuum chamber, and the machine components up to the crab cavities, have been implemented in the EicRoot GEANT simulation framework [2]. To make the simulations as realistic as possible the beam line element 3-dimensional locations and magnetic fields are directly taken from the MADX files used for optics calculations. Their apertures precisely reflect our present understanding of how these magnets can be built in reality. The vacuum system is modeled by importing the essential part of the engineering design into GEANT.

In the following, results from these simulations will be presented.

Realization of the Scientific Requirements for the Central Detector

A shown in figure 3.1, the beam element free region L^* along the beam lines is $\pm 4.5\,\mathrm{m}$ from the IP. In order to have the acceptance required for inclusive and semi-inclusive DIS as well as exclusive reactions it is critical to reconstruct events over a wide span in pseudo-rapidity ($-4 \leq \eta \leq 4$), as discussed in section **??**. Therefore the design of the vacuum system in the detector volume (see Figure 3.6) needs to fulfill these specifications:

- Provide enough space to pass the synchrotron radiation fan through the detector.
- Do not extend beyond a 2° opening angle from the interaction point.

Figure 3.8 shows the integration of the various detector components around the beam pipe elements in the outgoing hadron beam direction, overlaid by a deep inelastic electron-deuteron scattering event with the secondary particle tracks and hits in the TPC and the silicon trackers.

Realization of the Scientific Requirements for the Interaction Region

Exclusive Processes
As emphasized below the detection of forward-going scattered protons from exclusive reactions as well as of neutrons from the breakup of heavy ions in incoherent and non-diffractive reactions is particularly challenging.

Electron-Proton Scattering: Extreme care has been taken to transport protons with $0.2\,\mathrm{GeV/c} < p_T < 1.3\,\mathrm{GeV/c}$ through the IR such that they can be detected as soon as they

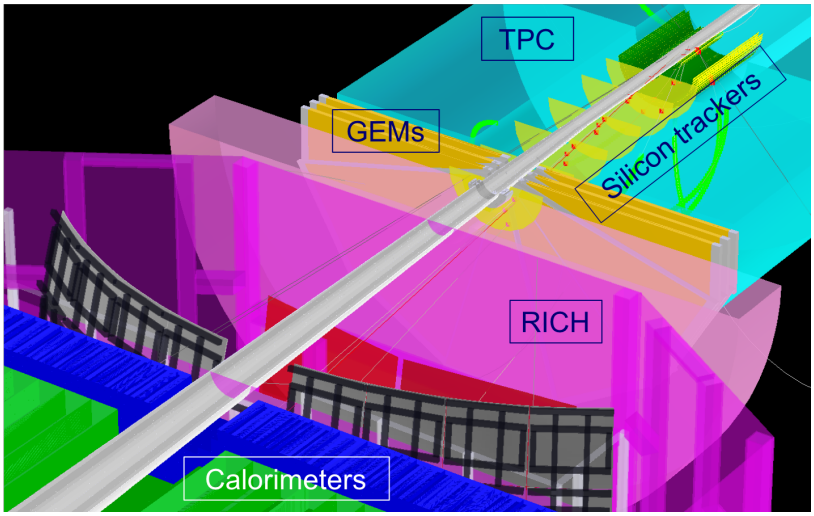

Figure 3.8: The integration of the beam pipe and various detector components in the outgoing hadron beam direction.

can be separated from the core of the beam. To achieve this p_T coverage over a wide range of center-of-mass energies a multi-prong approach is required. Protons with scattering angles up to 5 mrad are detected in the Roman Pots, while the range from 6 to 20 mrad is covered by the B0 large-acceptance spectrometer (see Sec. **??** for more details). In general the main detector starts seeing secondary particles above ~ 30 mrad ($\eta \sim 4$), and bending power of the 3 T solenoid is sufficient for momentum measurement above ~ 50 mrad ($\eta \sim 3.5$ or so).

The current Roman Pot configuration has two stations each with 2-5 silicon planes at 26.1 m and 28.1 m downstream of the IP, with a relatively modest single point XY-resolution. As shown later, even this very basic setup provides sufficient acceptance and a good momentum and scattering angle measurement.

There are several effects influencing the low p_T acceptance. We have been following the general rule of thumb that the distance between the inner edge of the Roman Pot silicon sensors and the beam orbit should be 10σ in X and Y. The physical size of the separation $\sigma_{x,y} = \sqrt{(\beta_{x,y}\epsilon_n)/\gamma}$ is driven by the normalized beam emittance ϵ_n and the β-functions $\beta_{x,y}$ at the location of the Roman Pots. The acceptance at large p_T is mainly constrained by the magnet apertures, vacuum system, and the overall size of the electron quadrupole magnet, which shares the bore of the B0pf containing the B0 spectrometer.

Figure 3.10 summarizes the p_T acceptance for three different proton beam energies, $E_p =$ 41 GeV, 100 GeV, and 275 GeV for the "high beam divergence optics" (see Table 3.6) for the EIC for the case of e+p DVCS events. In this case, the longitudinal momentum fraction of the scattered proton with respect to the beam, x_L, is $x_L > 0.8$, where the lower values come from events with $Q^2 > 50\text{GeV}^2$. The figures illustrate the need for a multi-prong detector approach to provide the full p_T acceptance over a wide range of hadron beam energies. For $E_p = 41$ GeV the limiting factor in acceptance at high p_T is the inner dimension of

the vacuum chamber and the magnet apertures. At $E_p = 100\,\text{GeV}$ one in general has full acceptance in p_T but there exists some "grey" (transition) area separating the forward scattered proton acceptances in the B0 spectrometer and the Roman Pots. We are currently investigating how much of this "grey" area can be filled by optimizing the layout of the outgoing vacuum beam pipe, or potentially having more space between the hadron beam pipe and electron quadrupole inside the B0pf bore. For $E_p = 275\,\text{GeV}$ the acceptance is mainly limited at low p_T, however this region can be partly filled by taking data with the "high acceptance beam optics" (see Table 3.6) for the EIC, which reduces the beam envelope size at the Roman Pot location and consequently relieves the 10σ separation cut, as illustrated in the x-y acceptance plots in Fig. 3.9.

Parameter	High Divergence	High Acceptance
RMS norm. emit., h/v [μ]	4.6/0.75	4.9/0.62
β^*, h/v [cm]	90.0/4.0	395.0/4.0
RMS $\Delta\theta$, h/v [μrad]	132/253	65/229

Table 3.6: Table of selected beam parameters for high divergence and high acceptance beam optics configurations for 275 GeV protons with strong hadron cooling. The increased β^* and from high divergence to high acceptance subsequently decreases the beam envelope size at the Roman Pots, increasing the low-p_T proton acceptance. Angular divergence in the proton beam is also reduced in the high acceptance configuration, reducing its contribution to smearing of the reconstructed transverse momentum.

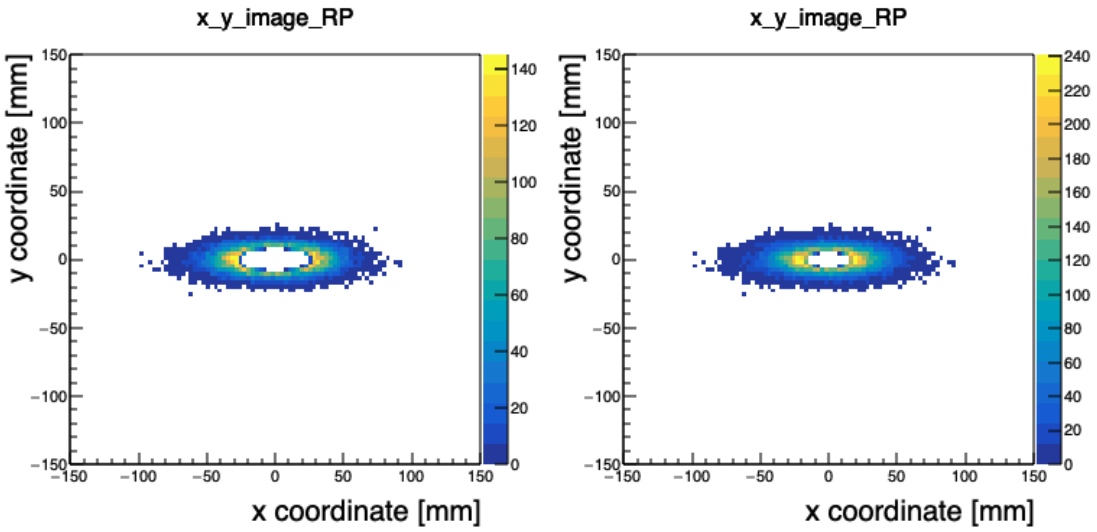

Figure 3.9: Acceptance image of protons from 18x275 GeV e+p DVCS events using the high divergence (left) and high acceptance (right) optics configurations. The transverse beam size, σ, at the Roman Pots decreases by a factor of 2 when going from the high divergence to high acceptance configuration, which increases the acceptance of low-p_T protons.

The p_T resolution of these forward scattered particles is of equal importance as their acceptance. There are several effects that can influence the momentum resolution and need

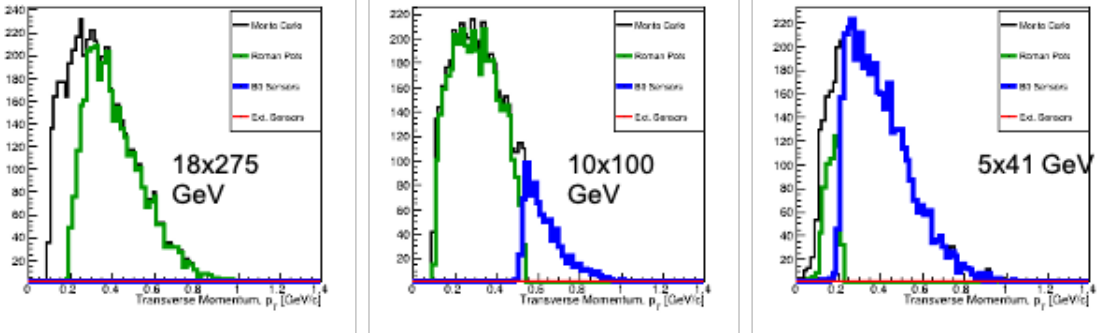

Figure 3.10: p_T acceptance for DVCS protons in the Roman Pots (green) and B0 detectors (blue) for three different energy combinations. In the medium and low-energy configurations, both the Roman Pots and B0 are required to cover the full acceptance. At high energy, the low-p_T acceptance is limited by the optics configuration which determines the size of the beam at the Roman Pots location.

to be mitigated:

- The finite width of the vertex distribution at the IP adds uncertainty in the angle determination. This uncertainty can be eliminated by determining the vertex of the event through other tracks in the event being registered in the main detector and benefit from the excellent vertex definition from the μ-vertex detector.
- The finite pixel size of the sensors used for the proton reconstruction impose uncertainty of the hit location, and therefore potentially smear the reconstructed momentum of the particle. This can be mitigate by choosing pixels for the silicon sensors of a reasonably small pitch.
- The angular divergence $\sigma_\theta = \sqrt{\epsilon_n/(\beta^*\gamma)}$ of the beam, which directly leads to a smearing of the scattering angle.
- The hadron bunch "rotation" at the IP due to the crab cavities. Crabbing implies a transverse momentum kick $p_x(z)$ to the particle bunch, with the kicking strength proportional to the longitudinal position z of particles in the bunch. Therefore at the IP particles at the "head" of the bunch will have a slightly different orientation and/or transverse offset compared to the ones in the "tail" of the bunch, which leads to additional smearing of the apparent scattering angle. The z-vertex determination of the event provided by the main tracker as well as high-resolution timing of the Roman Pot silicon sensors (of an order of $\sim$ 35 psec or so) is able to fully mitigate this effect.
- The spread in the beam energy, which normally has a width (RMS) of $\sim 10^{-4}$.

The track reconstruction is based on a Kalman filter (either with or without the vertex constraint) for the protons registered in the B0 spectrometer and a matrix transport method (with the realistic beam envelope size at the IP) for the protons registered in the Roman

Pots. Under relatively conservative assumptions one obtains a p_T resolution as low as $\sim 15 - 50\,\mathrm{MeV/c}$ for reconstructed protons in the far-forward region with all smearing effects included.

Electron-(heavy)Nuclei Scattering: The only possible way to tag exclusive electron-nucleus events for heavy nuclei is to veto the nuclear break-up. Figure **??** shows the break-up neutron momentum vs. scattering angle in the laboratory frame for different beam energies. One needs to transport neutrons within a cone of 4 mrad to 6 mrad, depending on the beam energy, through the IR to a Zero-Degree Calorimeter (ZDC). The ZDC is placed right in front of the B2APF magnet at $\sim 30\,\mathrm{m}$ from the IP. Figure 3.11 (left) shows the layout of the beam elements towards the ZDC. The picture illustrates that currently neutrons are not really well centered at the $60 \times 60\,\mathrm{cm}^2$ ZDC front surface. This is improved by the new IR design. Preliminary estimates show that the new option provides sufficient containment of the hadronic shower for the whole ZDC angular acceptance from of 0 to 4 mrad.

Figure 3.11 shows the resulting acceptance for neutrons from nuclear break-up. The required angular acceptance of ± 4 mrad has been achieved and even extended beyond that by careful consideration of machine beam line element apertures.

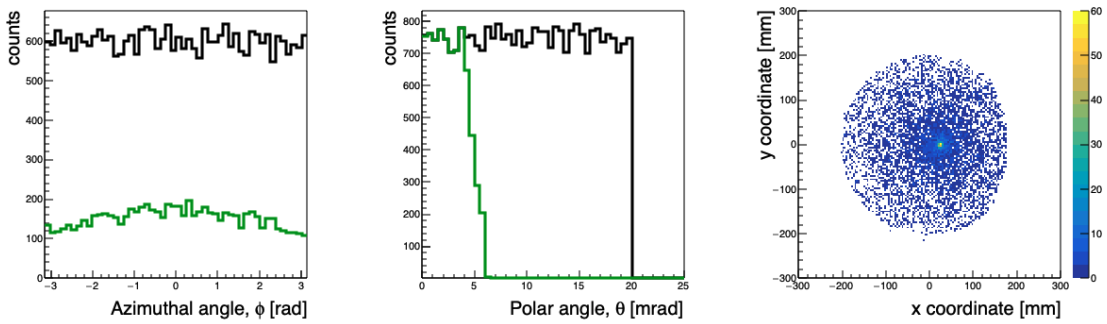

Figure 3.11: Plots of the neutron azimuthal angle, ϕ, acceptance (left), polar angle, θ, acceptance (middle), and an image of the hits on the ZDC (right) with the axes representing the assumed 60cm x 60cm size of the proposed detector in the far-forward region. These neutrons were generated with a particle gun to illustrate the neutron acceptance with the restriction of the aperture size, which generally only allows neutrons to be accepted up to about 4.5 mrad, with slightly better acceptance up to 5.5 mrad, asymmetric in ϕ

Electron-(light)Nuclei Scattering:

The physics program of an EIC requires proton and neutron collisions to allow for a full flavor separation of parton distribution functions. As neutron beams are not feasible, (un)polarized ^{3}He and deuteron beams are used for these purposes. To ensure the scattering really occurred off the neutron the spectator proton(s) need to be detected. Figure 3.12 shows the momentum, azimuthal, and polar scattering angle for the spectator protons (top) and active neutrons (bottom) from incoherent diffractive J/ψ electron-deuteron

events for deuterons with $E_D = 135\,\text{GeV/n}$. This study was carried out using the BeAGLE e+A Monte Carlo event generator, with the full GEANT4 simulation of the far-forward IR region, detailed in [3]. The detection of the spectator protons in e+D scattering requires an additional detector system because the spectator proton has approximately half the rigidity of the deuteron beam. This means the protons will be bent outside of the beam pipe after the B1apf dipole magnet. Inclusion of so-called "off-momentum detectors" will allow for detection of these spectator protons. Fig. 3.13 shows the same setup, but for the case where the neutron is the spectator. In the case where the proton is the active nucleon, the larger scattering angle places those protons into the acceptance of the B0 spectrometer, while the active neutrons have a reduced acceptance due to the cutoff of the acceptance because of the aperture. Additionally, the active protons have a larger range of x_L and therefore more protons are severely off-momentum and lost in the quadrupoles, as seen in the top-middle panel of Fig. 3.13.

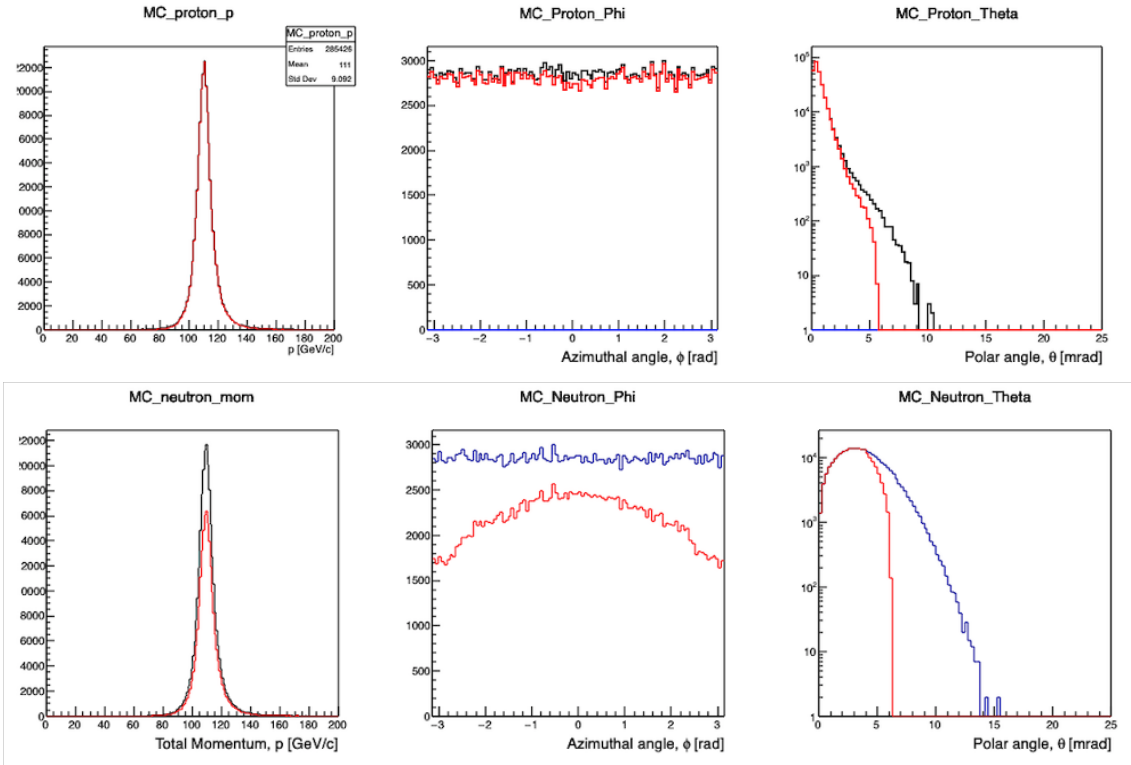

Figure 3.12: 3-momentum p, azimuthal angle (ϕ), and polar angle (θ) acceptance for protons (top) and neutrons (bottom) for the proton spectator case.

Because of the complicated acceptances for scattered protons from various processes, it is instructive to analyze the proton acceptance as a function of proton momentum and scattering angle for a fixed beam energy (or fixed far-forward magnet settings). This essentially probes the dependence on the longitudinal momentum fraction (x_L) of far-forward proton acceptance. Fig. 3.14 depicts the resulting momentum, polar angle, and azimuthal angular acceptance for scattered protons assuming 275 GeV proton beam settings, but with protons ranging in momentum from 0.0 to 275.0 GeV/c.

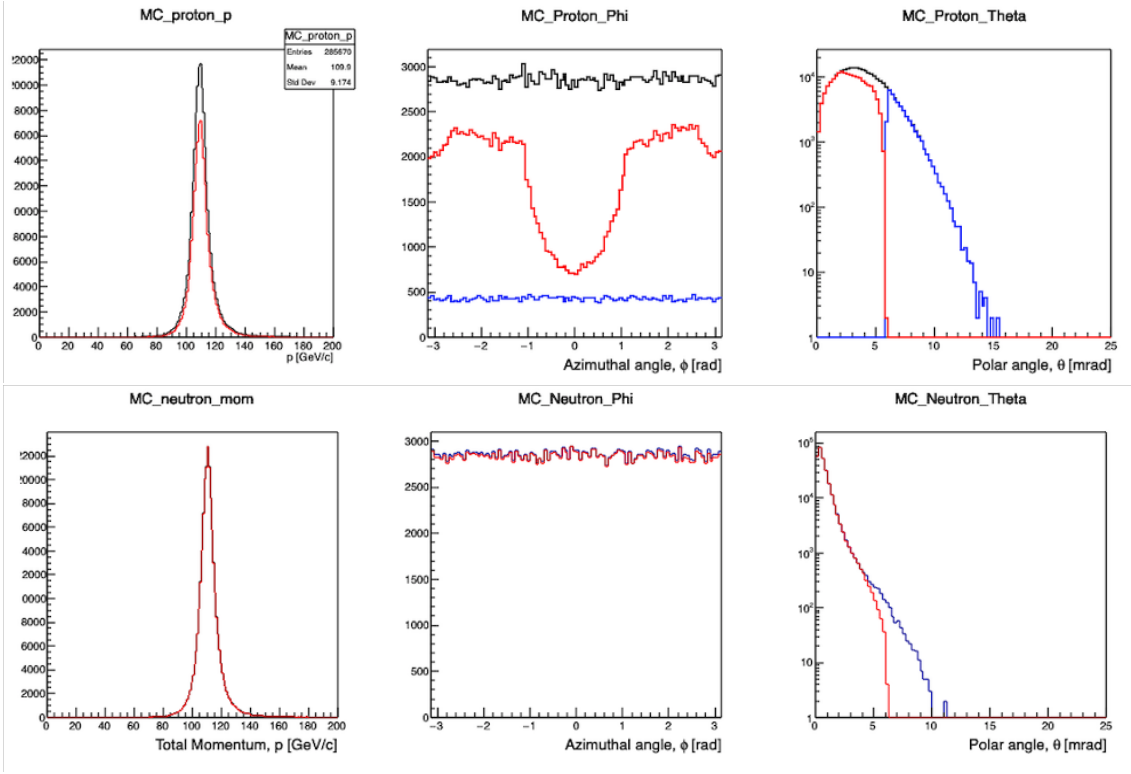

Figure 3.13: 3-momentum p, azimuthal angle (ϕ), and polar angle (θ) acceptance for protons (top) and neutrons (bottom) for the neutron spectator case. The additional blue line in the top-middle, and top-right panels shows the impact of the B0 spectrometer in covering the large angle acceptance.

Inclusive Processes:

Many physics topics beyond the ones discussed in the EIC White Paper [4] benefit from tagging the scattered electrons at Q^2 values significantly below $1\,\mathrm{GeV}^2$. Scattered electrons with $Q^2 < 0.5\,\mathrm{GeV}^2$ cannot be detected in the main detector. Therefore, similar to the HERA collider detectors, a special low-Q^2 tagger is needed. In this case, we consider two independent low-Q^2 taggers as shown in Fig. 3.15. The taggers should include calorimeters for triggering and energy measurements, and they should be finely segmented to disentangle the multiple electron hits per bunch crossing from the high rate bremsstrahlung process. The taggers should also have position sensitive detectors, such as silicon planes, to measure the vertical and horizontal coordinates of electrons. The combined energy and position measurements allow reconstruction of the kinematic variable Q^2 and x_{BJ}. If the position detectors have multiple layers and are able to reconstruct the electron direction this will over-constrain the variable reconstruction and improve their measurement; this may also provide some measure of background rejection.

Tagging of low-Q^2 processes provides an extension of the kinematic range of DIS processes measured with electrons in the central detector. It crosses the transition from DIS to hadronic reactions with quasi-real photons. An example of acceptance as a function of

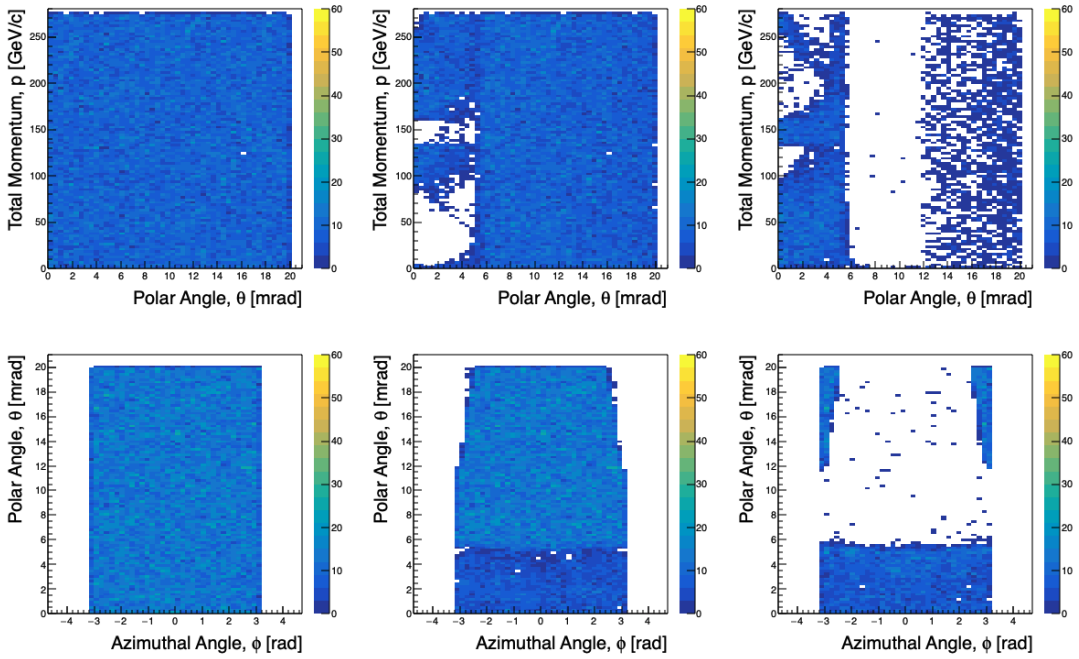

Figure 3.14: Distributions for generated protons (left), reconstructed protons (middle), and the difference between the two (right) for momentum vs. polar angle (top row) and polar angle vs. azimuthal angle (bottom row). These distributions show the combined for the three proton detector subsystems, as well as effects of asymmetric loss of protons in the lattice quadrupoles (for the off-momentum detectors), and asymmetric loss of protons due to the placement of the electron quadrupole within the B0pf magnet bore.

Q^2 and electron energy, E_e is shown for the two taggers in Fig. 3.16. The acceptance for the full Q^2-range including measurements with the central detector and electron taggers as depicted in Fig. 3.15 is shown in Fig. 3.17.

Electrons with energies slightly below the beam are bent out of the beam by the first lattice dipole after the interaction point. The beam vacuum chamber must include exit windows for these electrons. The windows should be as thin as possible along the electron direction to minimize energy loss and multiple scattering before the detectors.

The preliminary conclusion of these physics simulation studies is that the current IR design fulfills most of the requirements summarized in Table **??**. Several potential improvements to the design are identified already, which will extend the EIC physics reach even further.

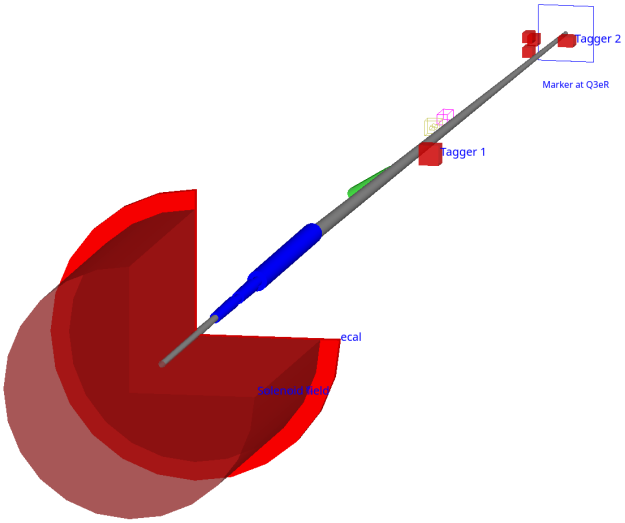

Figure 3.15: A view along the outgoing electron beam from the main detector towards the low-Q^2 tagger and luminosity monitor.

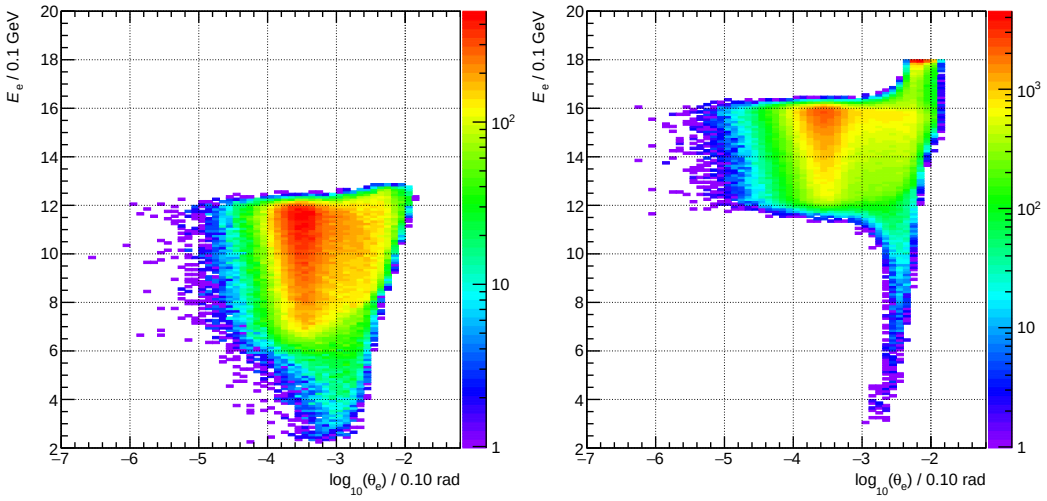

Figure 3.16: Scattered electron energy E_e and polar angle θ_e for events of quasi-real photoproduction with a hit in Tagger 1 (left) or 2 (right).

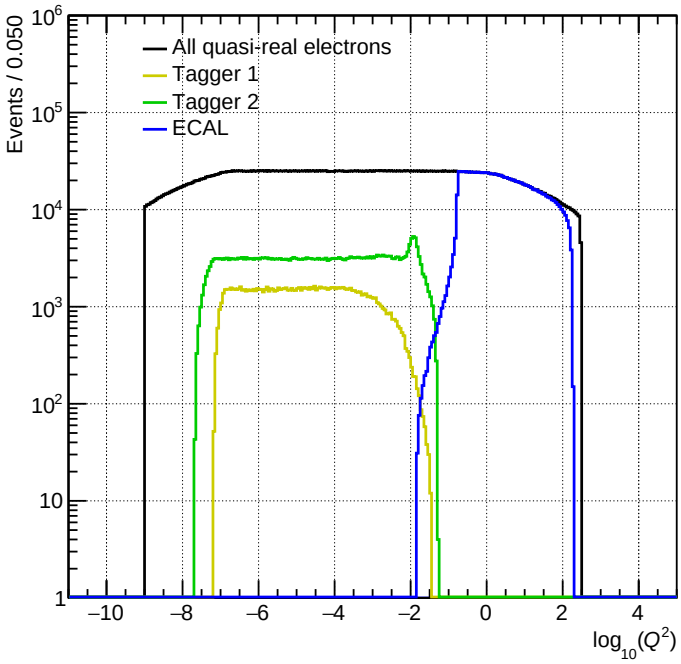

Figure 3.17: Coverage in Q^2 for tagger detectors and ECAL.

3.1.4 Crab Cavity Requirement and Specifications

EIC Crab Cavity Introduction

Robert Palmer introduced the concept of crab cavity as a countermeasure to the geometric reduction in luminosity caused by the crossing angle in colliders [5]. Crab cavity imparts a transverse momentum kick $p_x(z)$ to the particle bunch, with the kicking strength proportional to the longitudinal position z of the particle. At the right phase, the bunch arrives at the cavity with its center particle receives an accumulative zero deflection. The transverse momentum kick can be expressed as

$$p_x(z) = \frac{eE_0}{\omega}\sin(kz)\sin\left(\frac{kL}{2}\right)\sin\phi_{crab} \approx \frac{eE_0 z}{c}\sin\left(\frac{kL}{2}\right)\sin\phi_{crab}$$

where E_0 is the amplitude of the electric field acting on the bunch, ω and k are the angular frequency and the wave number of the crab cavity respectively, L is the bunch length, and ϕ_{crab} is the phase advance of the crab cavity. The longitudinal coordinate z is referencing to the center of the bunch, where $z = 0$.

For beam energy of E_b, transverse oscillation translates the longitudinally dependent kick p_x to a transverse offset x_{IP} at the interaction point (IP), which gives

$$x_{IP} = R_{12}\frac{p_x c}{E_b} = \sqrt{\beta_{crab}\beta^*}\frac{eE_0 z\sin\left(\frac{kL}{2}\right)\sin\phi_{crab}}{E_b}$$

where R_{12} is the element of transverse transfer matrix from the crab cavity to the IP, β_{crab} and β^* are the beta functions at the crab cavity and IP.

At desired cavity voltage, the transverse offset will cancel the crossing angle in the optics and restore the head-on collision. The requirement to the transverse offset can be exchanged with the crossing angle as

$$\theta_c = \frac{2x_{IP}(z)}{z} = \sqrt{\beta_{crab}\beta^*}\frac{2eE_0\sin\left(\frac{kL}{2}\right)\sin\phi_{crab}}{E_b}$$

The required crabbing voltage should be

$$V = \frac{cE_b\theta_c}{2e\omega\sqrt{\beta_{crab}\beta^*}\sin\phi_{crab}}$$

EIC Crab Cavity Requirement and Specifications

The eRHIC crossing angle is in the horizontal direction. Given the current proton bunch length for EIC is 6 cm at high energy and 7 cm at low energy, in order to increase the beam

	Unit	proton horizontal	proton vertical	electron horizontal	electron vertical
ϵ_{rms}	nm	15.8	2.5	24	2.0
β_{crab}	m	1300	1300	150	150
safety factor		20	20	27	45
minimum diameter	cm	10.3	10.3	5.7	1.2

Table 3.7: Crab cavity system aperture diameter limitation at high energy case.

lifetime, a long wavelength of the crab cavity at low frequency is required to linearize the transverse kick within the proton bunch with respect to the longitudinal position, therefore reduces the synchro-betatron oscillation as well as the non-linearity in the bunch geometric shape. Consider the current SRF fabrication technology and the main frequency of the proton ring, the crab cavity frequency is chosen to be 197 MHz, which is the 2520th harmonic of the revolution frequency. A set of second harmonic crab cavities at 394 MHz is planned to be added to the main cavites for optimum performance. To minimize the design risk and single cavity fabrication cost, the electron beam will share the same design of the second harmonic crab cavities for the ions. Due to a much lower energy, the voltage required from the electron crab cavity system is about 60% of the voltage from the second harmonic ion crab cavity system. Thus, the crab cavity system development focused on the ion beam requirement, which would fulfill both beams, and recoginize the more stringent higher order mode damping for the electron beam. The detailed crab cavity RF designs are elaborated in detail in section **6.5.6**.

In addition, the beta function, together with the emittance e, determines the beam size σ_{crab} along the ring as shown in the equation below, and therefore sets limits on the aperture diameter d_{crab} for the crab cavity.

$$\sigma_{crab} = \sqrt{\epsilon_{rms}\beta_{crab} + D^2\delta_{rms}^2}$$

where ϵ_{rms} is the rms emittance, D is the dispersion function, and $\delta_{rms}$is the energy spread. In the case of EIC, $D\delta_{rms}$ is negligible. The crab cavity system minimum aperture is determined based on the beam size multiplied by a safety factor for each beam. Each requirement is listed in Table 3.7 respectively. The aperture of the crab cavity system is chosen to meet the larger required diameter of both directions in the same ring. The large emittance during low energy operations can be compensated by a smaller beta function at the crab cavity site to maintain the same bunch size for the aperture.

Table 3.8 shows the crab cavity related lattice parameters and the calculated voltage requirement for each scenario. The table also compares the EIC crab cavities with the existing crab cavities from KEKB and Hi-Lumi LHC [6–8]. The Hi-Lumi Large Hadron Collider (LHC) project introduced two novel designs of compact crab cavities for proton beam. The Hi-Lumi LHC shares a similar bunch length as the EIC, and same frequency as the 2nd

	KEKB		Hi-Lumi LHC	EIC		
Parameter	LER	HER	both	proton		electron
Full crossing angle [mrad]	22	22	0.59	25		25
Energy [GeV]	3.5	8	7000	275		18
RMS bunch length [cm]	0.7	0.6	7	6		0.9
Frequency [MHz]	509	509	400	197	394	394
Wave number	10.6679	10.6679	8.3834	4.13	8.26	8.26
Wave length [m]	0.5890	0.5890	0.7495	1.52	0.76	0.76
Scheme	global		local	local		
6σ of wavelength	0.07	0.06	0.56	0.24	0.47	0.07
β at IP [m]	1.2	1.2	0.15	0.9		0.59
β at crab cavity [m]	51	122	2616	1300		150
Horizontal beam size [μm]	110	110	7	119		135
Piwinski angle [rad]	0.70	0.60	2.95	6.30		0.79
Voltage [MV]	0.92	1.36	12.43	33.83	-4.75	2.21

Table 3.8: Comparison of crab cavity parameters.

harmonic crab cavities in the EIC proton ring. Therefore, the LHC crab cavity program can directly benefit the EIC in many aspects from design through out commissioning.

The location of the crab cavity is chosen with consideration of minimizing the voltage, i.e. maximizing the beta function. However, the dispersion functions and their derivatives at the crab cavity locations are non zero for both rings, which would generate linear and non-linear instabilities with beam-beam interaction. Analysis of the detailed beam dynamics with crab crossing for is discussed in section 4.4.2.

The spacial allowance for crab cavity system installation is limited by the distance between the electron and the ion beam lines in horizontal direction, and the local structures in the vertical plane, e.g. cable trays, cryogenic transfer lines, and the tunnel floor, but the limitation is much more relaxed compared to the LHC requirement. The parallel beam lines can accomodate the crab cavity cryomodules with 70 cm radius. In the meantime, the IR is a popular region for various species of magnets, instrumentation devices, along with their auxilaries. With the current matching lattice, the crab cavity systems are given 15 meters of longitudinal installation space on both sides of the IP for hadron beam to provide the total deflecting voltage, and 4 m for electron beam. **Figure 3.18 shows the crab cavity cryomodules installed in both rings on one side of the IP, and the RSC ring is also shown in the picture. The red tunnel illustrates the injection line tunnel for hadron beam.** The location of the crab cavity cryomodule starts after 40 m on both sides to the interaction point (IP) for hadron beam, and resides in the similar region for electron beam. These

limits are well considered at the beginning of the cavity, coupler, helium vessel, tuner and cryomodule development to avoid any significant change in the future.

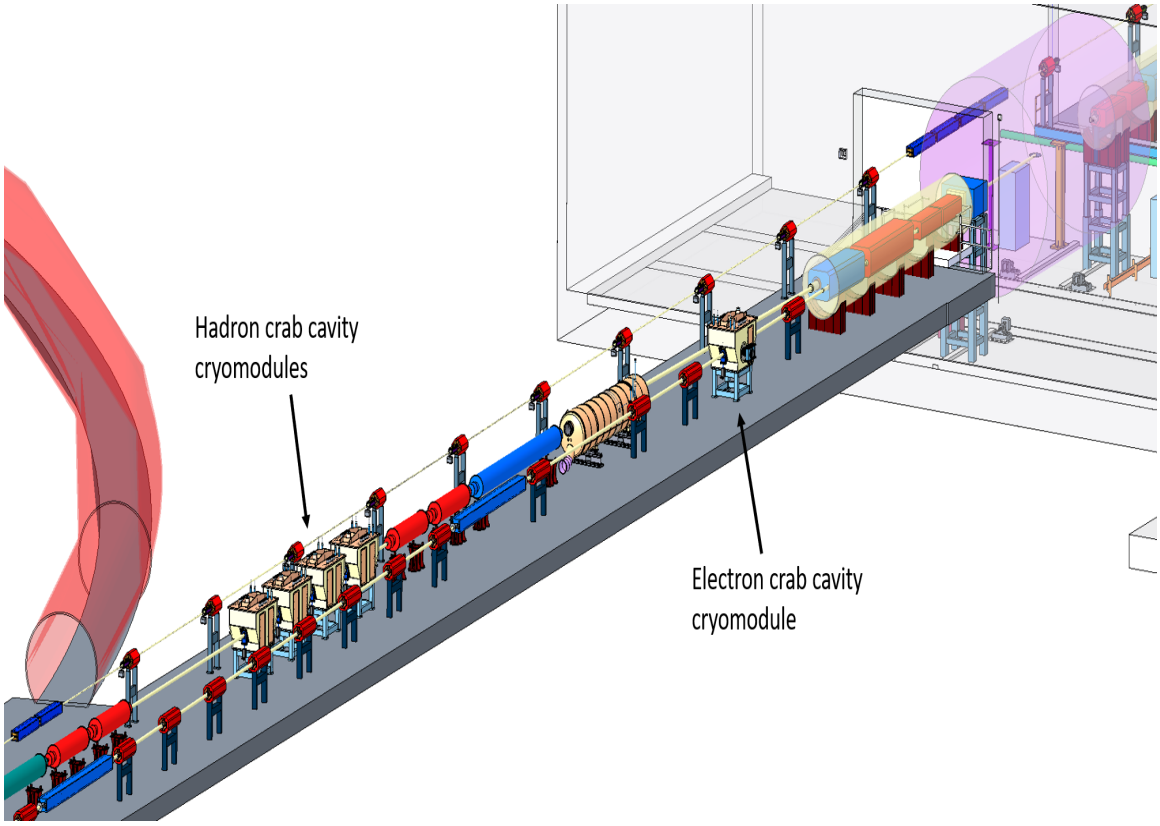

Figure 3.18: Schematic drawing of the local configuration of all beam lines near the crab cavity installation region.

3.1.5 Impedance Modeling

The main parameters used to evaluate the collective effects of the electron beam are given in Table 3.9. To estimate instability thresholds, the wake-potential for a 0.3 mm bunch length was used for beam dynamics simulations in the SPACE particle tracking code [9]. This simulated length is much shorter than the expected nominal bunch length of 19 mm for the unperturbed circulating beam.

Table 3.9: Parameters used for threshold calculation.

Parameter	Value
Energy E [GeV]	10
Revolution period T_0 [μs]	12.79
Momentum compaction α	1.45×10^{-3}
Energy loss U [keV]	9100
RF voltage V [MV]	41
Synchrotron tune ν_s	0.0815
Damping time τ_x, τ_s [ms]	70, 35
Energy spread σ_δ	5.5×10^{-4}
Bunch length σ_s [mm]	19

IR Chamber

The vacuum chamber geometry for the interaction region (IR) is very complex with abrupt changes in the cross section as the particle beams cross each other. A cross-sectional top view of the preliminary IR chamber is shown in Figure 3.19 (upstream) and Figure 3.20 (downstream). Figure 3.21 shows a sectional view of the upstream section of the IR chamber.

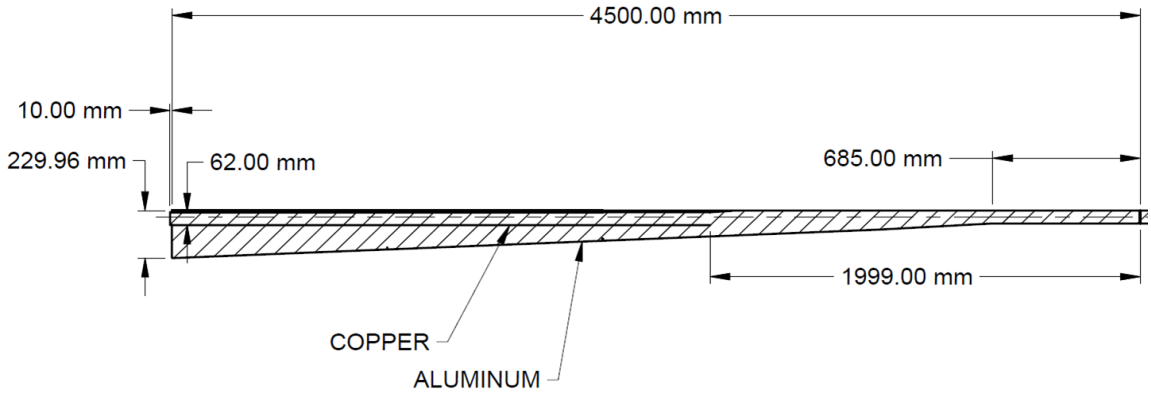

Figure 3.19: Cross-sectional top view of the upstream IR chamber.

The IR chamber design has been iterated on several times since the EIC pCDR. One of the major contributions to the local impedance are discontinues where the electron and hadron beam pipes merge. The electron pipe geometry needs to be designed so it does not block the propagation of forward moving particles resulting from collisions within a 25 mrad cone starting from the interaction point. This requirement complicates the transition be-

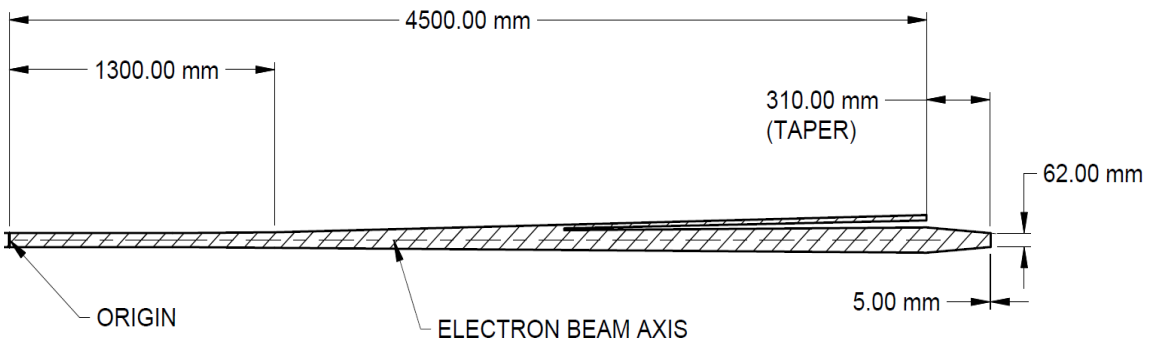

Figure 3.20: Cross-sectional top view of the downstream IR chamber.

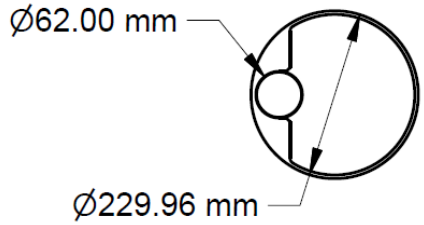

Figure 3.21: Section view of the upstream IR chamber entrance. The electron beam chamber with a 62 mm diameter.

tween the two beam pipes. As a first attempt, the electron beam pipe with a diameter 2d=62mm was grounded to the hadron pipe with a small taper angle (see Figure 3.22). Half of the taper was left open. This arrangement results in a cavity type structure between the area of the electron pipe grounding and the larger hadron beam pipe. The initial taper length was chosen to be 30 mm. The results are shown in Figure 3.24 and labeled 'L=30 mm'.

To reduce the cavity effect, the electron beam pipe was extended, and a horizontal slot was added on one side to provide clearance for the particle propagation to the forward detector. The length of the taper was also increased to 90mm. These results are also shown in Figure 3.23 and are labeled "L=90 mm with slot". The longitudinal wakefield is presented in Figure 3.23a for a 0.3 mm bunch length (pseudo-Green's function). For L=90 mm, the short-range wakefield becomes inductive. Increasing the tapered transition helps to decrease the longitudinal impedance and the loss factor (Figure 3.23b and Figure 3.23d). The real part of the longitudinal impedance shows existence of the narrow-band impedance at low frequency, generated due to the horizontal slot. The imaginary part of the longitudinal impedance $ImZ_{||}$ divided by $n = \omega/\omega_0$, where $\omega_0 = 2\pi \times 78.186$ kHz, increases slightly.

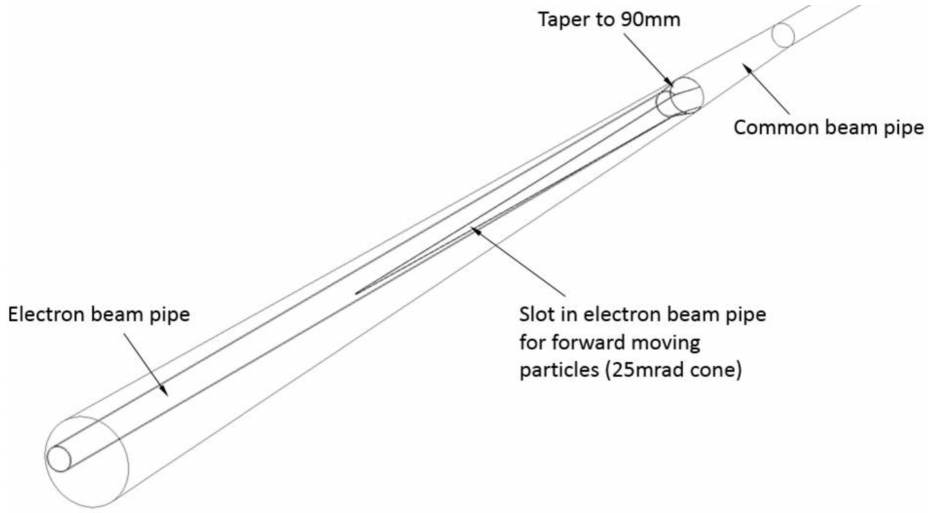

Figure 3.22: The EIC IR vacuum chamber design. Version 2

The tapered transition predominantly contributes to the high-frequency impedance. The resonance modes at frequency below 2 GHz, have been eliminated by lengthening the tapered transition. However, the horizontal slot contributes to the low-frequency impedance and $(ImZ_{||}/n)_0$ and becomes slightly larger at $f \to 0$ (Figure 3.23c).

Further refinement to the main detector chamber is shown in Figure 3.26. The electron beam pipe was extended all the way to the center of the detector chamber. This approach maintains the same diameter of the electron beam pipe and eliminates the need for a taper. An opening large enough for the forward moving collision particles is added to the side of the electron beam pipe. The summarized results are presented in Figure 3.27. The longitudinal wakefield is shown in Figure 3.27a and the real part of the longitudinal impedance is presented in Figure 3.27b. The low-frequency resonance modes around 3 GHz have been eliminated (Figure 3.27b) since there is no cavity formed between the two beam pipes. The loss factor has also been reduced to $k_{loss} = 2.2$ mV/pC for a bunch length of $\sigma_s = 12$ mm.

Using the machine parameters presented in Table 3.9 and the simulated results, the heat load due to multiple passes of the bunch train through the structure can be estimated by

$$P_{\text{loss}} = \kappa_{\text{loss}} I_{\text{av}}^2 T_0 / M, \tag{3.2}$$

where M is the number of bunches, T_0 is the revolution period, and I_{av} is the average current. Applying the expected average current $I_{av} = 2.48$ A, number of bunches $M = 660$ and the expected revolution period $T_0 = 12.79$ μs the total expected power loss $P_{loss} = 262$ W. This value can be reduced even further by doubling the bunch length. For a bunch length $\sigma_s = 24$ mm, the power loss factor drops by almost a factor of 10 to $k_{loss} = 0.2$ mV/pC resulting in a total power loss $P_{loss} = 30$ W.

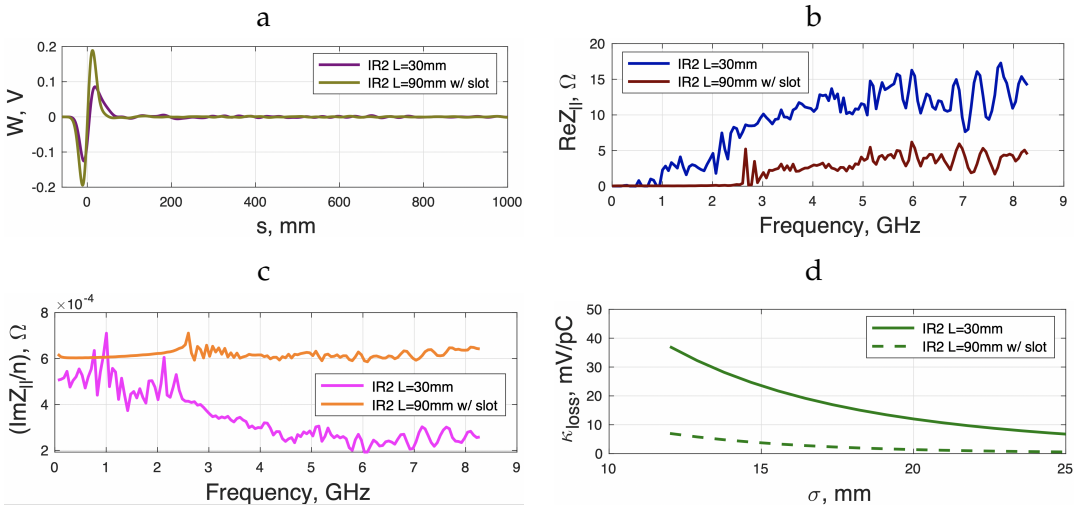

Figure 3.23: IR chamber summary results. a) The longitudinal wakepotential simulated for a $\sigma_s = 0.3$ mm bunch length and 1 pC charge. b) Real part of the longitudinal impedance up to $f = 350$ GHz. c) The imaginary part of the longitudinal impedance divided by $n = \omega/\omega_0$, where $\omega_0 = 2\pi \times 78.186$ kHz. d) The loss factor as a function of bunch length.

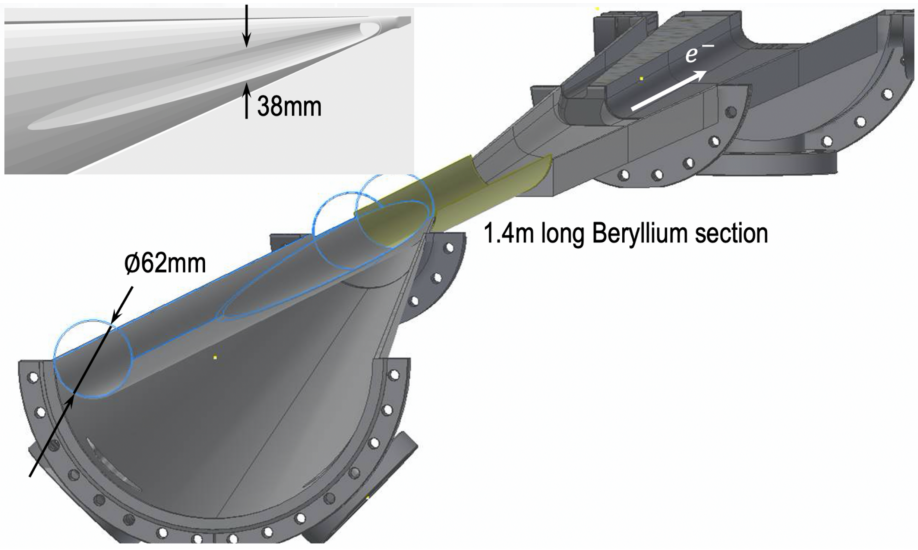

Figure 3.24: The EIC IR vacuum chamber design. Version 3.

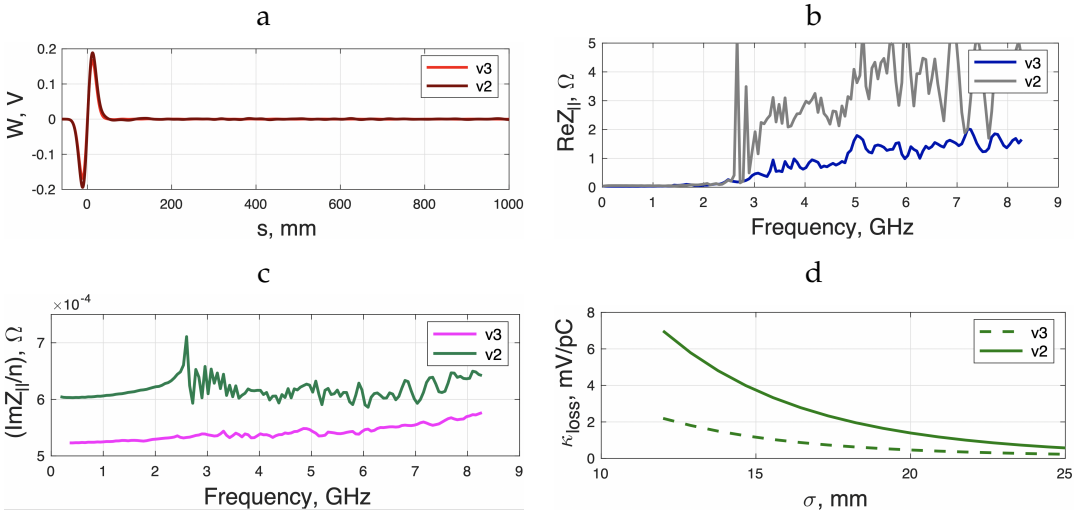

Figure 3.25: Summary results for IR chamber v3. a) The longitudinal wakepotential simulated for a $\sigma_s = 0.3$ mm bunch length and 1 pC charge. b) Real part of the longitudinal impedance up to f=350 GHz. c) The imaginary part of the longitudinal impedance divided by $n = \omega/\omega_0$, where $\omega_0 = 2\pi \times 78.186$ kHz. d) The loss factor as a function of bunch length.

Longitudinal Impedance Model

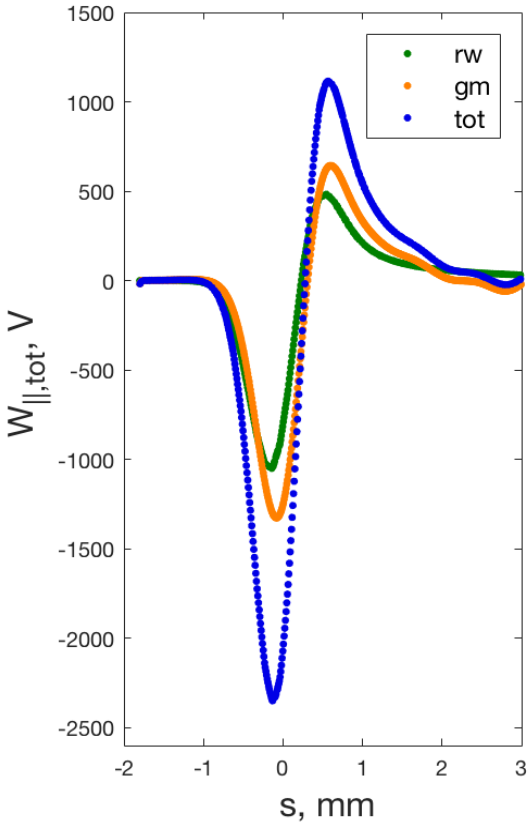

Figure 3.26: Longitudinal short-range wakepotential calculated for a bunch length of $\sigma_s = 0.3$ mm. The total longitudinal wakepotential of the EIC (blue trace) is a sum of the resistive wall contribution (green trace) calculated analytically (Equation 3.3) and the geometric wakepotentials (orange trace).

By passing through the vacuum chamber, the electron beam generates electromagnetic fields, which can affect the beam stability. This makes it important to determine the impedance/wakepotential for all of the vacuum components distributed around the ring. A list of preliminary vacuum components is presented in Table 3.10. The exact geometric dimensions and surface resistivity of many of the vacuum components have not been finalized yet. For a first pass analysis the wakepotential and impedances simulated for several of the NSLS-II vacuum components have been scaled using the EIC lattice parameters to study the instability thresholds. The geometric impedance due to the cross-sectional changes of the vacuum components has been calculated by the GdfidL code. Table 3.10 indicates the origin of the data which is being used for the applied wakepotential. As the storage ring geometry is finalized, updates to the simulations will be performed and used to generate the total impedance budget for particle tracking simulations and analytical evaluation. The contribution of the resistive wall to the total impedance is calculated

Table 3.10: List of the vacuum components contributing to the total impedance of the electron storage ring.

Object	Abbreviation	Qty	Project
Bellows	BLW	380	NSLS-II
LA BPM	LABPM	494	NSLS-II
Stripline	SL	18	NSLS-II
Gate Valve	GV	45	NSLS-II
Flange Absorber	FABS	200	NSLS-II
RF Cavity	CAV	23	NSLS-II
RF Tapered Transition	TPRDRF		NSLS-II
IR Chamber	IRCHM	1	EIC

separately by applying the analytical approach derived by Bane and Sands [10]:

$$W_{\parallel}(\tau) = \frac{r_e mc^2 N_e}{2b\sqrt{2\mu_r Z_0 \sigma_{\text{con}}}} i \left|\frac{\tau}{\sigma}\right|^{3/2} e^{-\tau^2/4\sigma^2} \times \left[I_{1/4}\left(\frac{\tau^2}{4\sigma^2}\right) - I_{-3/4}\left(\frac{\tau^2}{4\sigma^2}\right) - \text{sgn}(\tau) I_{-1/4}\left(\frac{\tau^2}{4\sigma^2}\right) + \text{sgn}(\tau) I_{3/4}\left(\frac{\tau^2}{4\sigma^2}\right) \right] \tag{3.3}$$

where b is the vacuum chamber radius, $Z_0 = 120\pi$ is the impedance of free space, σ is the electrical conductivity and μ_r is the relative permeability of the chamber surface. As a preliminary estimate for the resistive wall surface, six 257 m long arc sections and twelve 123 m long copper straight sections with a radius of 20 mm are assumed.

The total longitudinal wakepotential, which is a sum of the short-range geometric and resistive-wall longitudinal wakepotentials, is shown in Figure 3.26. The real part of the frequency spectrum of the total longitudinal impedance is presented in Figure 3.27 up to 350 GHz. The total longitudinal wakepotential $W_{\parallel,\text{tot}}$ was used as an input file for the SPACE particle tracking code along with the parameters presented in Table 3.9. Numerical simulations were done using 30 million macro-particles and 800 grid points in order to accurately determine the first microwave instability threshold and to characterize the microwave dynamics. The energy spread of the unperturbed Gaussian bunch at low current is estimated at $\sigma_\delta = 5.5 \times 10^{-4}$. From this the first microwave instability threshold is observed at $I_{\text{th}} = 4.5$ mA (see Figure 3.28), which is above the single bunch current of 3.8 mA. The bunch lengthening effect due to potential-well distortion (see Figure 3.28) is small enough up to 4 mA for the applied total longitudinal wakepotential.

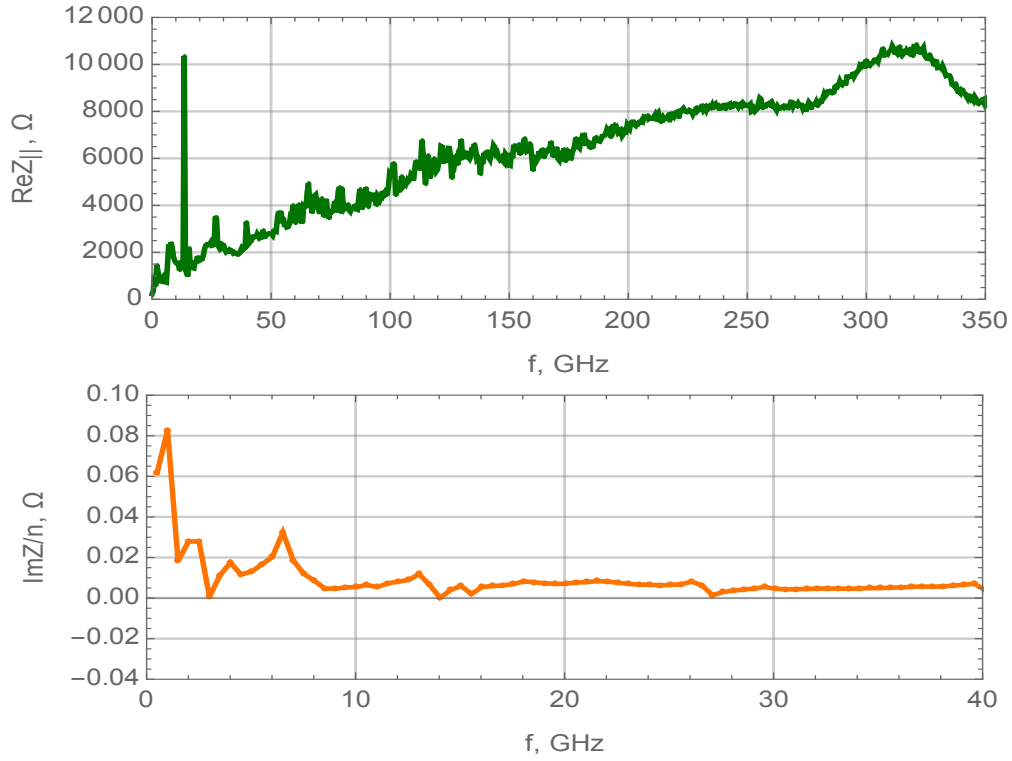

Figure 3.27: Top: Real part of the longitudinal impedance. Bottom: Imaginary part of the longitudinal impedance divided by $n = \omega/\omega_0$, where $\omega_0 = 2\pi \times 78.186\,\text{kHz}$.

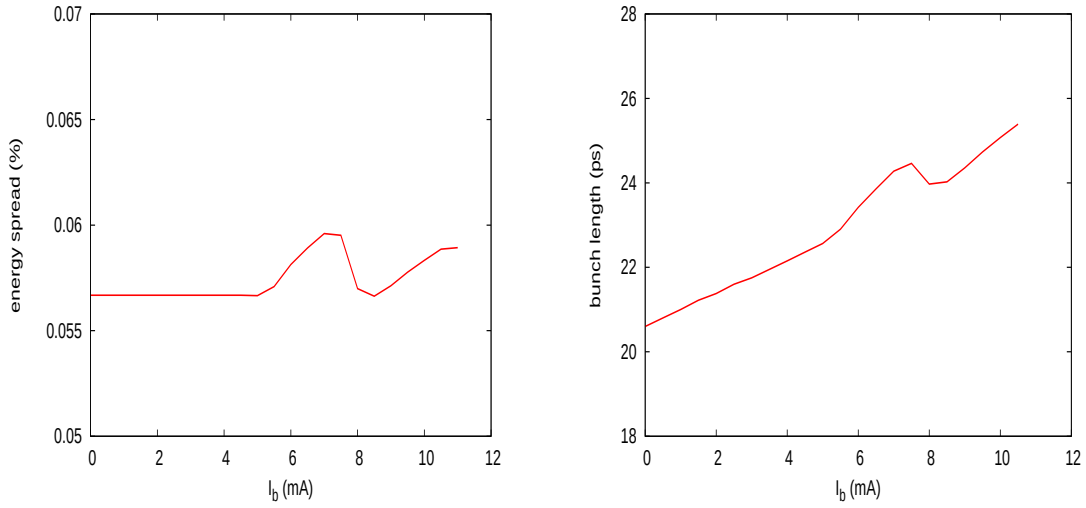

Figure 3.28: Left: Energy spread as a function of single bunch current. Right: Bunch lengthening dependence on the single-bunch current.

3.1.6 Synchrotron Radiation Analysis

The IR crossing angle scheme avoids the necessity of separator dipoles in or near the detector, which would generate a wide fan of hard synchrotron radiation photons. However, the nearby low-β quadrupoles generate a synchrotron radiation cone that can be equally harmful for different detector components, if not handled appropriately.

In contrast to the homogeneous fan produced by dipole magnets, the photon cone generated by quadrupoles consists of a huge number of weak photons in its center, and a comparatively small number of very high energy photons with increasing distance from the center. These high energy photons stem from electrons in the transverse tails of the beam distribution that experience strong magnetic fields at large amplitudes in these low-β quadrupoles. Additionally, since the beam-beam interaction tends to cause an overpopulation of the transverse electron beam tails, especially in the vertical plane, the number of hard photons produced in the quadrupoles by large-amplitude electrons can be significantly higher than expected for a pure Gaussian distribution. Therefore it is important to take all these factors into account when evaluating the synchrotron radiation background in the detector, and designing a masking scheme.

Nonlinear effects in the beam-beam interaction lead to the formation of non-Gaussian tails with an enhanced electron density. Figure 3.29 illustrates this. The colliding electron beam requires about 50% larger aperture than without beam-beam interactions. The magnets and synchrotron radiation masks have to provide sufficient aperture for these tails to pass through in order to provide beam lifetimes of several hours.

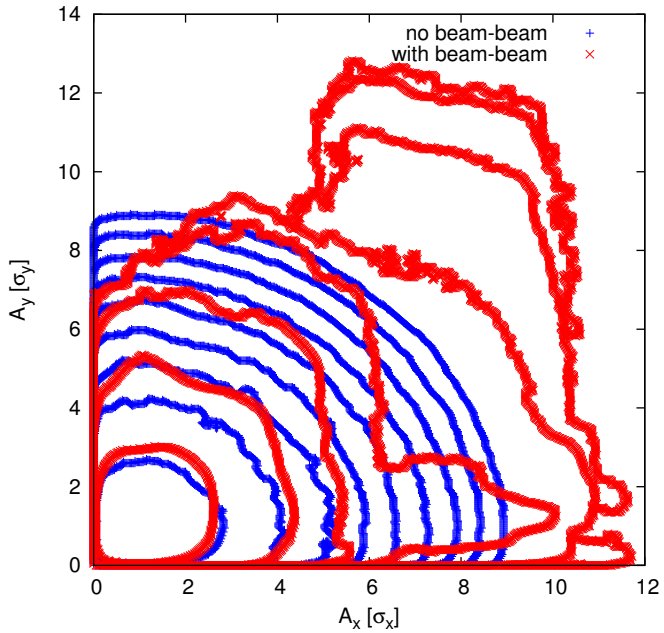

Figure 3.29: Transverse electron density distribution with (red) and without (blue) beam-beam interaction. The contour lines are spaced by a factor 10.

The design of an EIC general purpose detector requires a machine element free region of ± 4.5 m around the IP. As a consequence, any synchrotron radiation mask that gets hit by direct radiation can only be installed outside the detector volume in the incoming electron beam direction. The aperture of those masks has to be sufficiently large to ensure beam lifetimes on the order of several hours. As shown in Figure 3.29 the electron density at 13σ is about the same as at 8σ without beam-beam. Therefore, one expects a beam lifetime of more than 20 hours [11] with a 13σ aperture and beam-beam effects.

The first focusing element (quadrupole Q0EF) starts at a distance of 5.3 m from the IP. In order to reduce the peak magnetic fields encountered by electrons in the transverse tails, this magnet as well as the following quadrupole Q1EF are comparatively long; the length is limited by the requirement to interleave focusing elements in the hadron beam line [12]. Table 3.11 lists the design parameters of the last two quadrupoles upstream of the IP.

A dual stage masking scheme is what is required to limit the synchrotron radiation fan through the central detector. On the incoming side, its cross section will be identical to that of the masks before the central detector. Their size is determined by the 13σ beam size requirement at their specific location. Assuming radii of the upstream ellipse of 11 mm in the horizontal plane, and 10 mm vertically, at the downstream end of the central detector, the cone radii will have substantially increased, to 71 mm horizontally, and 19 mm vertically. This growth of the synchrotron radiation fan determines the minimum dimensions of the detector beam pipe that ensure strongly reduced background from primary photons generated by the electron beam.

In the next step, the impact of potentially backscattered photons on the detector is simulated using the code DESYNC [13].

The focusing upstream of the detector is designed to minimize the magnetic fields of the last two quadrupoles seen by electrons in the transverse tails of the beam. This is accomplished by designing quadrupoles Q1EF and Q2EF with a low gradient and an extended length. Even at the highest electron beam energy of 18 GeV this results in peak fields of only 0.3 T at the 15σ design aperture of these magnets. However, since the movable upstream mask at $s = 4.5$ m has an aperture radius of only 10σ, no electrons are present in the beam beyond this limit. Therefore, the maximum magnetic field sampled is only 2/3 of the peak field of those quadrupoles, namely $B_{\max} = 0.2$ T. The corresponding critical energy of the synchrotron radiation generated by the small number of electrons at the outer edges

Table 3.11: Electron IR magnet parameters on the upstream side of the detector, for the highest design energy of 18 GeV.

Magnet	s_i [m]	l [m]	IR [cm]	B [T]	g [T/m]
Q1EF	5.00	1.2	2.2	0.309	-14.1
Q2EF	8.74	1.72	4.85	0.282	6.0

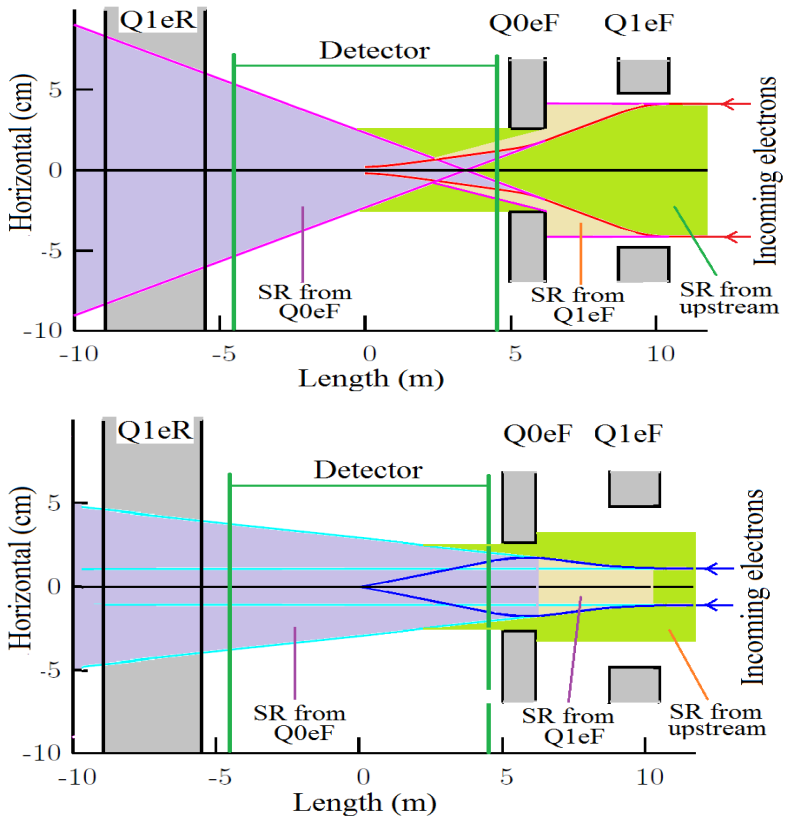

Figure 3.30: Synchrotron radiation fans from the low-β quadrupole doublet through the IR. Top: top view; Bottom: side view.

of the beam is therefore reduced to

$$E_c = \frac{3}{2}\frac{\hbar c^2 e E^2 B}{E_0^3} = 43.2\,\text{keV}, \tag{3.4}$$

at 18 GeV, or $E_c = 13.3$ keV at $E = 10$ GeV. Here $E_0 = m_e c^2$ is the electron energy at rest.

Photon scattering in the IR geometry described above has been simulated with the code DESYNC [13]. Assuming a detector beam pipe that is tailored to accommodate the primary synchrotron radiation fan according to Figure 3.30, the radiation load outside the 1 mm thick beryllium detector pipe reaches a maximum of 2.2 rad/hour at 18 GeV in the 1 m long section right after the mask, and less than a μrad/hour everywhere else throughout the central detector. At a beam energy of 10 GeV the maximum rate reduces by 2-3 orders of magnitude.

While these radiation levels are likely acceptable more detailed simulations including the actual EIC detector are required. These simulations are beyond the capabilities of DESYNC and will therefore be carried out using a simulation code such as GEANT4 [14].

The test particle Monte Carlo code SynRad, developed at CERN, has been used to determine the synchrotron radiation flux distribution in the interaction region due to the upstream dipole and last two quadrupoles. This code was used with an electron beam energy of 18 GeV and a beam current of 260 mA, 10 percent of which is distributed in tails as described earlier. The SynRad output has been used as input in two separate studies: the detector backgrounds expected due to photon flux on the beampipe, and interaction region vacuum studies as a function of beam dose.

For the detector occupancy studies, SynRad was used to generate photon trajectories and energies for photons likely to hit the beamline in the vicinity of the interaction region. To enhance the efficiency of this simulation, transparent planes were generated at a radius of 2.92 cm, 97 percent of the inside diameter of the Be central pipe. These test facets extended from 3.3 m upstream of the IR to -4 m downstream of the IR. Most photons that are incident on these test facets are traveling in a trajectory where they will intersect the wall and cause detector background.

The detector background studies were performed for several configuration: the March optics, the May optics with the final photon absorber at 390 cm, and the May optics with the final photon absorber at 350 cm. The photon data was input into full GEANT based detector simulation to generate expected detector backgrounds for all scenarios.

In addition, an independent program (called SYNC_BKG) used to study SR backgrounds that was developed at SLAC has also been applied to the EIC IR design. This program and has been used to study SR backgrounds for the SLAC B-Factory, the KEK B-factory, the SuperKEKB current B-factory, the FCCee design [15,16], the CEPC design, the ILC and the JLEIC design. The Programs (SynRad and SYNC_BKG) are in very good agreement. The total power numbers are in very close agreement and the total number of photons incident on a given surface also agree.

SYNC_BKG is derived from a program developed in the 1980s by Al Clark called QSRAD. The program was originally built to study a gaussian beam going through final focus magnets for colliders. SYNC_BKG has included in it the ability to introduce a non-gaussian beam tail that is described as a lower and wider gaussian and the ability to accept bend magnets. SYNC_BKG performs a grid integration of the transverse beam profile using weighted marco-beam particles at each grid point and tally up the photon hit rate and energy spectrum on selected beam pipe apertures that are used to model the IR beam pipe. The SR background study of the IR has pointed out the importance of the non-gaussian beam tail distribution. This non-gaussian distribution has several sources. Initially, when the accelerator is in the commissioning phase, the beam tail distribution is dominated by beam-gas interactions from around the entire ring (primarily Bremsstrahlung and Coulomb scattering). In this stage, the beam-beam effects mentioned above are not yet prominent as the luminosity and bunch currents are still low. As the accelerator collects more running time and the number of A-hrs increases, the beam pipe outgassing from SR begins to decrease and this reduces the beam-gas interactions. Then the beam-beam effects become a noticeable generator of non-gaussian beam tail particles as well as other bunch related interactions (i.e. Touschek scattering, Inter-Beam Scattering) and even the effects of luminosity in the form of radiative Bhabha scattering. All of these

effects populate the non-gaussian beam tail distribution and this quasi-stable distribution controls how close collimators settings can be before the beam lifetime becomes too short.

A very preliminary study of beam tail distributions indicate that the IR design as described should have acceptable background levels in the detector from SR at 18 GeV with electron non-gaussian beam tails that have approximately a 1-2 hour beam lifetime. This lifetime is defined by collimator settings that are placed at or near the Beam-Stay-Clear envelope. This includes back-scatter estimates from the IP face of the rear electron magnets as well as a preliminary calculation of the back-scatter rate from the beginning of the high-power SR surface located about 19 m downstream of the IP. A much more thorough study of the SR background for the detector is needed both at this energy of 18 GeV as well as at the beam energy of 10 GeV where the beam current is 10 times higher. This also includes a study of the SR background that will hit the very low Q^2 detectors foreseen to be near the beam in the downstream beam pipe. In addition, we have been and will continue to study the background experience of SuperKEKB as the accelerator is presently going through a startup and commissioning phase and is trying to take data at the same time. The background team of Belle II and SuperKEKB have done an enormous amount of work to classify and understand all of the background sources to date [17]. We will continue to draw on the experience gained by the SuperKEKB background team.

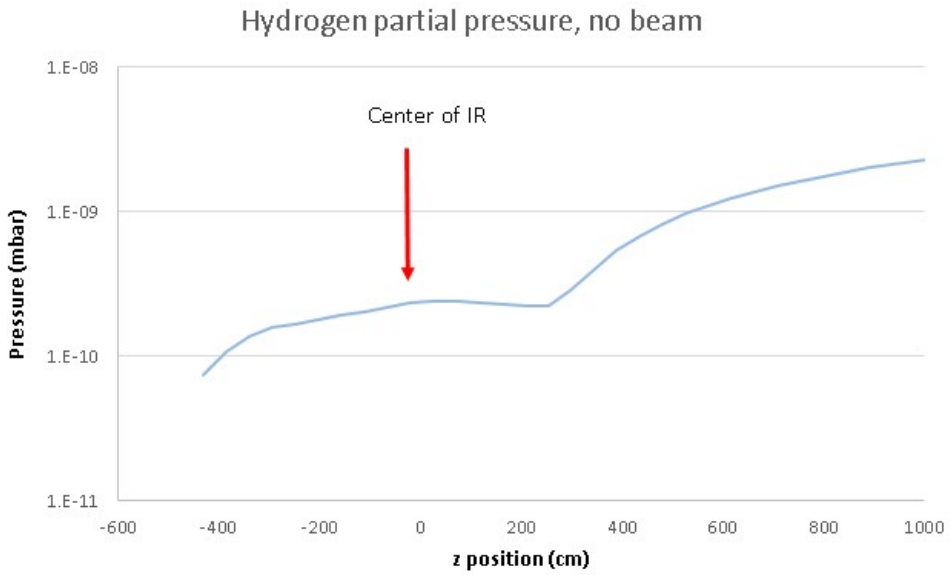

Figure 3.31: Molflow+ simulation of pressure distribution in the IR with no beam.

Molflow+ is a complementary code to SynRad, and can use the photon flux on each facet of a model in conjunction with experimental flux per dose rates measured from common vacuum materials to predict the pressure distribution in a system as a function of AmpHours. The pressure distribution for the interaction region vacuum system was first calculated in Molflow+ using the geometry shown in the next section, using an out-gassing rate of $1x10^{-12}$ mbarL/scm^2, and the pump speed and geometry as shown in Figure 3.31. For this first iteration, water vapor outgassing was not considered, and the electron beam is

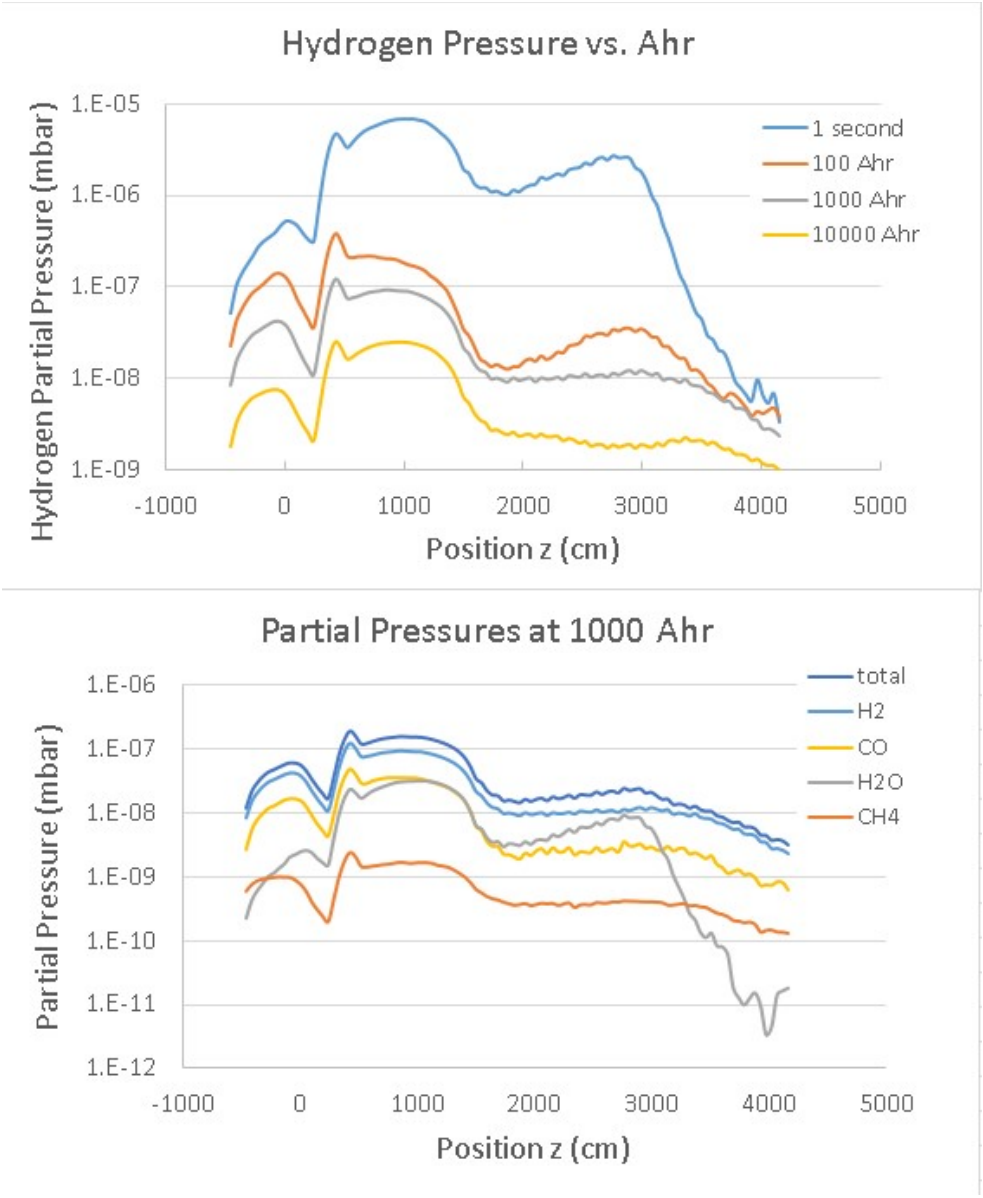

Figure 3.32: top: Pressure evolution vs. conditioning time in AmpHours for hydrogen. bottom: The expected gas composition for a conditioning time of 1000 Ahr.

traveling in the -z direction in these simulations. The calculated pressure distribution for the system without beam yields an interaction region pressure in the 10^{-10} mbar range.

To calculate the pressure that is expected with electron beam in the region, the output for the flux on each facet, as calculated by SynRad, can be imported into Molflow. Molflow then will use this photon flux and a library of Photon Stimulated Desorption (PSD) yield vs. beam dose. For hydrogen desorption from aluminum, the PSD rate starts at 0.01 hydrogen molecules desorbed per incident photon until a dose of $4x10^{-18}$ photons/cm^2, then

falls in a power law distribution with time. Molflow will use the dose per facet to calculate PSD induced outgassing on each facet of the model, and determine pressure distributions. In addition to hydrogen, the partial pressures of H2O, CH4 and CO can be calculated for the system.

The results of these coupled SynRad and Molflow+ simulations are shown in Figure 3.32. In all cases, the May geometry has been used, and combination NEG-ion pumps are in the model at the ends of the interaction region as shown in CAD layouts. In addition, a series of smaller NEG-ion pumps distributed along the incoming electron beamline to provide pumping between the final electron dipole before the IR where there is a significant synchrotron radiation load. The hydrogen partial pressure vs. dose is shown in the top graph, and the gas composition at 1000 Ahr is shown in the bottom graph.

References

[1] "SynRad+ is part of the MolFlow+ code from CERN, which traces photons to calculate flux and power distribution on a surface caused by synchrotron radiation."

[2] EicRoot simulation framework, `http://svn.racf.bnl.gov/svn/eic/eicroot`.

[3] Z. Tu, A. Jentsch, M. Baker, L. Zheng, J.-H. Lee, R. Venugopalan, O. Hen, D. Higinbotham, E.-C. Aschenauer, and T. Ullrich, "Probing short-range correlations in the deuteron via incoherent diffractive J/ψ production with spectator tagging at the EIC," 5 2020.

[4] A. Accardi *et al.*, "Electron Ion Collider: The Next QCD Frontier," *Eur. Phys. J.*, vol. A52, no. 9, p. 268, 2016.

[5] R. B. Palmer, "Energy Scaling, Crab Crossing, and the Pair Problem," in *High energy physics in the 1990's: Proceedings*, vol. C8806271, pp. 613–619, 1988.

[6] T. Abe *et al.*, "Beam operation with crab cavities at KEKB," in *Proceedings, 22nd Particle Accelerator Conference, PAC'07, Albuquerque, USA, June 25-29, 2007*, vol. C070625, p. 1487, 2007.

[7] K. Akai *et al.*, "Commissioning and Beam Operation of KEKB Crab RF System," in *RF superconductivity. Proceedings, 13th International Workshop, SRF 2007, Beijing, China, October 14-19, 2007*, 2007.

[8] P. Baudrenghien, A. Macpherson, R. Calaga, V. Parma, E. Jensen, E. Montesinos, O. Capatina, and K. Brodzinski, "Functional Specifications of the LHC Prototype Crab Cavity System," Tech. Rep. CERN-ACC-NOTE-2013-003, 2013.

[9] G. Bassi, A. Blednykh, and V. Smaluk, "Self-consistent simulations and analysis of the coupled-bunch instability for arbitrary multibunch configurations," *Phys. Rev. Accel. Beams*, vol. 19, no. 2, p. 024401, 2016.

[10] K. L. F. Bane and M. Sands, "The Short-Range Resistive Wall Wakefields," *AIP Conf. Proc.*, vol. 367, pp. 131–149, 1996.

[11] Piwinski, A, "Beam losses and lifetime," in *CERN Accelerator School*, CERN, 1985.

[12] C. Montag *et al.*, "Overview of the eRHIC Ring-Ring Design," in *Proceedings, 8th International Particle Accelerator Conference (IPAC 2017): Copenhagen, Denmark, May 14-19, 2017*, p. WEPIK049, 2017.

[13] S. Khan, unpublished.

[14] S. Agostinelli *et al.*, "GEANT4: A Simulation toolkit," *Nucl. Instrum. Meth.*, vol. A506, pp. 250–303, 2003.

[15] G. Voutsinas *et al.*, "FCC-ee interaction region backgrounds," *Int. J. Mod. Phys. A*, vol. 35, no. 15n16, p. 2041009, 2020.

[16] A. Abada *et al.*, "FCC-ee: The Lepton Collider: Future Circular Collider Conceptual Design Report Volume 2," *Eur. Phys. J. ST*, vol. 228, no. 2, pp. 261–623, 2019.

[17] P. Lewis *et al.*, "First Measurements of Beam Backgrounds at SuperKEKB," *Nucl. Instrum. Meth. A*, vol. 914, pp. 69–144, 2019.